IOP Publishing Phys. Med. Biol. 63 (2018) 215009 (22pp) https://doi.org/10.1088/1361-6560/aae5c9

Physics in Medicine & Biology

PAPER

RECEIVED
2 July 2018

REVISED
18 September 2018

ACCEPTED FOR PUBLICATION
2 October 2018

PUBLISHED
24 October 2018

# Two-dimensional noise reconstruction in proton computed tomography using distance-driven filtered back-projection of simulated projections

Martin Rädler[1,4], Guillaume Landry[1,4], Simon Rit[2], Reinhard W Schulte[3], Katia Parodi[1] and George Dedes[1,5]

[1] Department of Medical Physics, Ludwig-Maximilians-Universität München, 85748 Garching b. München, Germany
[2] Université de Lyon, CREATIS, CNRS UMR5220 Inserm U1044, INSA-Lyon, Université Lyon 1, F69373 Lyon, France
[3] Division of Radiation Research, Loma Linda University, Loma Linda, CA 92354, United States of America
[4] Authors contributed equally.
[5] Author to whom correspondence should be addressed.

**E-mail:** g.dedes@physik.uni-muenchen.de

**Keywords:** proton CT, variance reconstruction, distance driven binning, FMpCT, FFMCT, Monte Carlo Simulation

## Abstract

We present a formalism for two-dimensional (2D) noise reconstruction in proton computed tomography (pCT). This is necessary for the application of fluence modulated pCT (FMpCT) since it permits image noise prescription and the corresponding proton fuence optimization. We aimed at extending previously published formalisms to account for the impact of multiple Coulomb scattering (MCS) on projection noise, and the use of filtered back projection (FBP) reconstruction along curved paths with distance driven binning (DDB).

2D noise reconstruction for a beam of protons with parallel initial momentum vectors, and for projections binned both at the rear tracker and with DDB, was established. Monte Carlo (MC) simulations of pCT scans of a water cylinder were employed to generate pCT projections and to calculate their noise for use in 2D noise reconstruction. These were compared to results from an analytical model accounting for MCS for rear tracker binning as well as against the previously published central pixel model which ignores MCS. Image noise reconstructed with the formalism for rear tracker binning and DDB were compared to MC results using annular regions of interest (ROIs).

Agreement better than 8% was obtained between the noise of projections calculated with MC simulation and our model. Noise from annular ROIs agreed with our noise reconstructions for rear tracker binning and DDB. The central pixel model ignoring MCS underestimated projection and thus image noise by up to 40% towards the object's edge.

The use of DDB decreased the image noise towards the object's edge when compared to rear tracker binning and yielded more uniform noise throughout the image. MCS should not be neglected when predicting image noise for pixels away from the center of an object in a pCT scan due to the increasing influence of the gradient of the object's hull closer to the edges.

## 1. Introduction

Relative proton stopping power (RSP), the ratio of the proton stopping power of a given material to that of water at a given energy, is necessary for most clinical dose calculation methods used in proton therapy. RSP is currently estimated by x-ray computed tomography (CT) scans in clinical practice (Taasti *et al* 2018). The conversion from photon attenuation coefficients to RSP contributes considerably to range uncertainties (Paganetti 2012, Yang *et al* 2012). The potential of reducing these uncertainties by direct RSP measurements at the treatment position has motivated the recent revival of proton computed tomography (pCT), which was first proposed by Cormack in the early 1960s (Cormack 1963). Modern pre-clinical pCT scanners measure the positions and residual energies of the protons behind (and in some designs also in front of) the patient in a series of projections, from which an RSP image can be reconstructed (Penfold *et al* 2009, 2010, Rit *et al* 2013, Poludniowski *et al* 2014,

© 2018 Institute of Physics and Engineering in Medicine

Hansen *et al* 2016). Many groups are known to be designing, building or operating pCT (or heavier ion CT) prototypes (Rinaldi *et al* 2013, Sadrozinski *et al* 2016, Taylor *et al* 2016, Meyer *et al* 2017, Tanaka *et al* 2018) and initial reports of RSP accuracy support these endeavours (Giacometti *et al* 2017).

The concept of fluence field modulation computed tomography (FFMCT), initially suggested for x-ray CT by Graham *et al* (2007) and pioneered by the Toronto (Bartolac *et al* 2011, Bartolac and Jaffray 2013) and Madison groups (Szczykutowicz and Mistretta 2013a, 2013b), allows the tailoring of the spatial distribution of image noise and dose by modulating the x-ray fluence within a given CT projection. Fluence modulation has been realized by employing a digital beam attenuator (Szczykutowicz and Mistretta 2014), the binary collimator of a Tomotherapy machine (Szczykutowicz *et al* 2015), multiple aperture devices (Stayman *et al* 2016) or piecewise-linear dynamic attenuators (Shunhavanich *et al* 2018). While fluence modulation capability is crucial in achieving FFMCT, a mathematical model relating x-ray fluence and image noise and/or radiation dose is required to optimize the FFMCT fluence pattern (Bartolac *et al* 2011). Several publications cover the theory of noise reconstruction for x-ray CT for parallel (Huesman *et al* 1977, Gore and Tofts 1978, Huesman 1984, Kak and Slaney 1988, Buzug 2008a), fan (Wunderlich and Noo 2008) and cone beam (Zhang and Ning 2008, Shäfer *et al* 2015) acquisitions.

Clinical implementation of FFMCT would thus rely on prior imaging data to generate a patient model, which would be used as input to algorithms predicting noise projections required for noise reconstruction (Bartolac *et al* 2011). The patient model could thus be established on the basis of prior diagnostic imaging studies or even using an atlas.

Dedes *et al* (2017) proposed adapting FFMCT to proton computed tomography (pCT) scans acquired with pencil beam scanning (PBS) beamlines found in modern proton therapy facilities. While they could show the feasibility of fluence modulated pCT (FMpCT) in a simulation study, they relied on a 'forward planning' approach where simple geometric considerations guided a binary fluence modulation on a pencil beam by pencil beam basis. The same approach was employed for the recent experimental realization of FMpCT using the proton tracking phase II pCT prototype of the Loma Linda University and University of California Santa Cruz (Dedes *et al* 2018). Further developments in FMpCT thus require the modeling of the relation between proton fluence and pCT image noise to allow using an optimization strategy where pencil beam fluence could be continuously adjusted to achieve image noise prescriptions.

Preliminary work by Schulte *et al* (2005) for the noise of the central pixel in a pCT image of a water cylinder, using proton projections binned at the rear tracker, laid the groundwork for noise reconstruction in pCT. However, Schulte *et al* (2005) did not account for the impact of multiple Coulomb scattering (MCS) near object edges, and was published prior to the development of state of the art filtered back projection (FBP) along most likely paths (MLP) (Rit *et al* 2013), which makes use of distance driven binning (DDB) to create depth dependent projections for which rear tracker binning is a special case. As we will present in this paper, these effects have a non-negligible, non-trivial impact on two-dimensional (2D) image noise in pCT.

The goal of this paper was thus to realize 2D noise reconstruction for simulated pCT scans of a water cylinder, assuming an ideal version of proton tracking pCT scanners, and accounting for the impact of MCS and the distance driven binning (DDB) which underpins FBP along MLPs. To do so, we extended the FBP along most likely paths to allow noise reconstruction, and made use of projection noise calculated on the basis of Monte Carlo (MC) simulations of ideal pCT scans, as well as from a dedicated analytical model.

## 2. Material and methods

### 2.1. MC simulation and geometry

In order to validate the noise reconstruction methods presented in the following sections, a MC simulation of a pCT scan of a water cylinder with a diameter of 25 cm was carried out, assuming ideal detectors (see figure 1). We chose a 260 mm $\times$ 50 mm rectangular proton field covering the whole diameter of the cylinder and 50 mm along the cylinder's axis. The fluence of the beam was chosen to be 200 protons mm$^{-2}$, all protons were launched perfectly parallel with random starting positions from the source plane, and the initial proton energy ($E_{\mathrm{in}} = 250$ MeV) was monoenergetic. The proton path was tracked on two parallel planes on the front and rear side of the water cylinder (see figure 1 for the details of the geometry), perpendicular to the incident beam, returning the initial and final position and momentum direction of each proton along with their exit energies.

The simulation platform was based on Geant4 version 10.01.p02 (Agostinelli *et al* 2003). The reference physics list QGSP_BIC_HP was used for the simulation of the interaction of particles with matter, which relies on G4EmStandardPhysics for electromagnetic interactions. MCS is modeled via the G4WentzelIVIModel (Ivanchenko *et al* 2010). The tabulation of energy loss, range and inverse range, which are calculated during initialization, are done with 84 bins. More details on the energy loss are described in GEANT-Collaboration *et al* (2016).

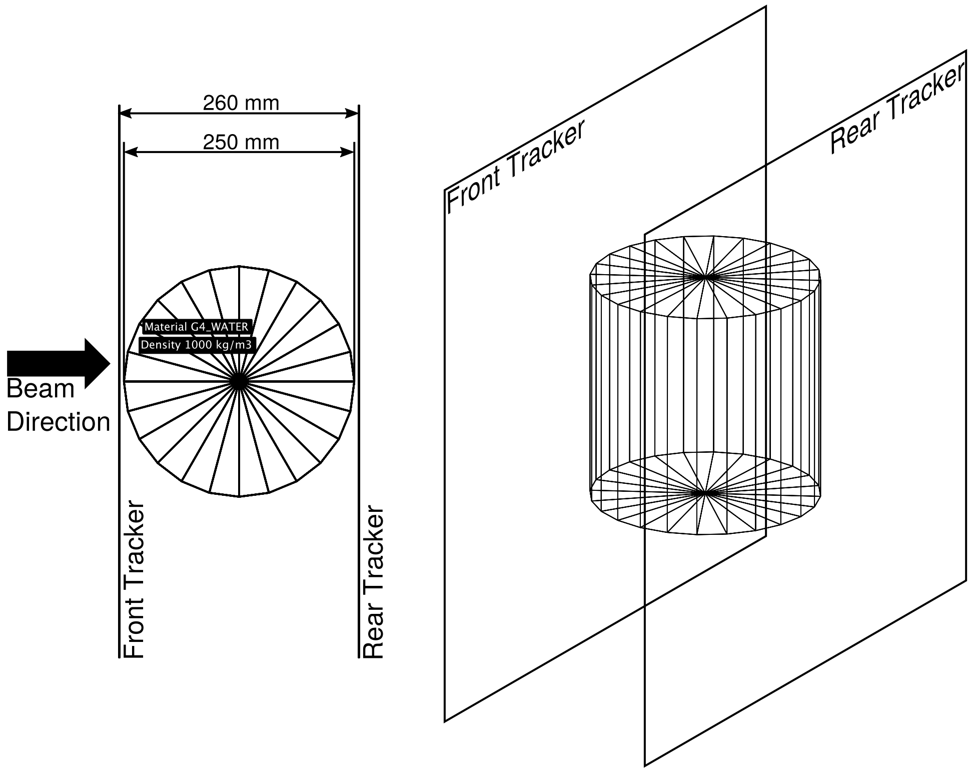


**Figure 1.** Geometry of the MC simulation.

### 2.2. Noise reconstruction formalism for pCT

Literature refers alternatively to noise images (one standard deviation, $\sigma$) or variance images ($\sigma^2$), with similar naming at the projection level. In this paper, we have opted to systematically employ the term noise reconstruction, which implies the trivial step of taking the square root of variance reconstructions. The noise reconstruction formalism presented below applies for pCT images reconstructed through distance driven binning (DDB), which was introduced by Rit *et al* (2013). By doing so, one is able to include the influence of MCS, as protons traversing curved paths will be binned into different detector pixels at different binning depths. The fluence modulation approach, as proposed by Dedes *et al* (2017), is based on parallel pencil beam irradiation. Therefore, we will solely discuss the parallel beam case in 2D slices.

After a brief summary of the image reconstruction (section 2.2.1), we will review the quantification of noise in the pCT projections (section 2.2.2) followed by the noise reconstruction of pCT binned at the rear tracker (section 2.2.3). The noise reconstruction including DDB is shown thereafter, given the noise projections binned at variable depth (section 2.2.4). We discuss the calculation of noise projections binned at the rear tracker in section 2.3.1 and with DDB in section 2.3.2.

#### 2.2.1. Image reconstruction

The coordinate system used in this paper is illustrated in figure 2. The FBP of an image slice $f(x, y)$, given the discrete projection values $p_{\gamma_n}(m\Delta\xi)$ acquired at discrete angles $\gamma_n$ with a $\Delta\xi$ spacing on the 1D projection grid using a discrete number of projections $N_p$, is given by

$$f(x, y) = \frac{\pi}{N_p} \sum_{n=1}^{N_p} h_{\gamma_n}(x\cos(\gamma_n) + y\sin(\gamma_n)), \tag{1}$$

where $h_\gamma(j\Delta\xi)$ are the convolved projections

$$h_{\gamma_n}(j\Delta\xi) = \Delta\xi \sum_{m=-D/2}^{D/2-1} p_{\gamma_n}(m\Delta\xi) g((j-m)\Delta\xi). \tag{2}$$

We chose the simplest convolution kernel from Ramachandran and Lakshminarayanan (1971) (Ram-Lak), which results from band limiting the ramp kernel

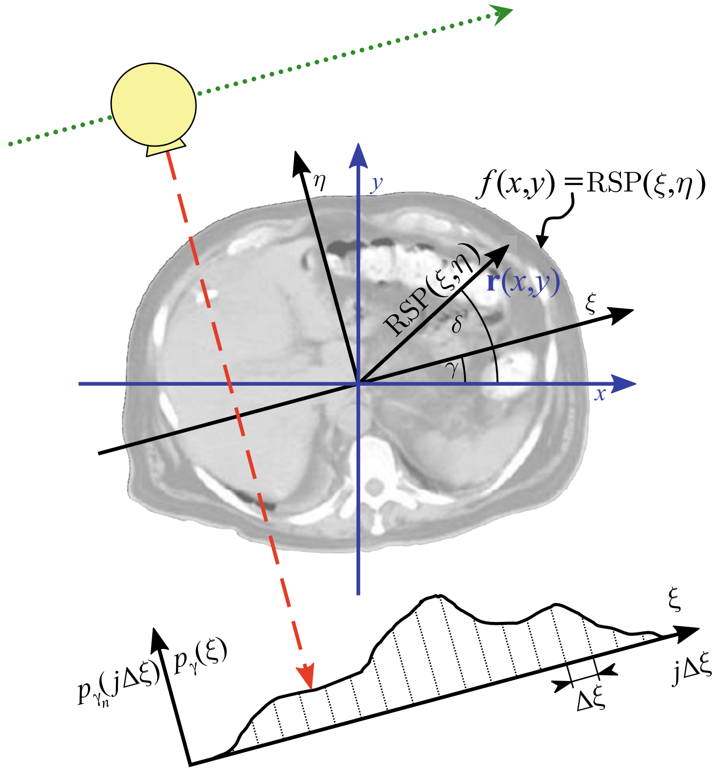


**Figure 2.** Setup of the acquisition and the coordinate systems. The source (yellow circle) moves along the dotted green line in order to generate one projection. Please note that this is an oversimplification in the context of pCT. Adapted by permission from Buzug (2008b).

$$g(j\Delta\xi) = \begin{cases} 1/(2\Delta\xi)^2 & \text{for } j = 0, \\ 0 & \text{for } j \text{ even } (j \neq 0), \\ -1/(j\pi\Delta\xi)^2 & \text{for } j \text{ odd.} \end{cases} \tag{3}$$

For a reconstruction using a given image pixel grid, with the pixel centers located at $(x_p, y_p)$, the convolved projections of equation (1) require interpolation, as the sampled projection values do not necessarily coincide with the sample points $\xi_n(x_p, y_p) = x_p \cos(\gamma_n) + y_p \sin(\gamma_n)$. Interpolation reduces the noise and should be taken into account, when estimating noise in reconstructed images from noisy projection images (Huesman *et al* 1977, Kak and Slaney 1988). For a linear interpolation between the two adjacent pixels $j$ and $j+1$, the complete reconstruction from the FBP becomes

$$f(x_p, y_p) = \frac{\pi}{N_p}\Delta\xi \cdot \sum_{n=1}^{N_p} \sum_{m=-D/2}^{D/2-1} p_{\gamma_n}(m\Delta\xi)\left\{g((j-m)\Delta\xi)\cdot[1-u] + g((j+1-m)\Delta\xi)\cdot u\right\}, \tag{4}$$

where both $j = j(\xi_n)$ and the weights $u = u(\xi_n)$ are determined by the location of the query point relative to the two adjacent projection sample values

$$u(\xi_n) = \frac{\xi_n - j\Delta\xi}{\Delta\xi}. \tag{5}$$

### *2.2.2. Statistical limitations of the acquisition*

Proton tracking pCT reconstruction with FBP relies on binning individual protons into projection pixels. For regular FBP (i.e. non-DDB), this can be done by using the data from the rear or front trackers. For FBP along most likely paths based on DDB, the paths of individual protons are reconstructed and protons are binned into projections with variable $\eta$ (see figure 2) (Rit *et al* 2013).

After binning the protons into their respective pixels, one calculates their water equivalent path length (WEPL) through

$$\mathrm{WEPL}_i = \int_{E_{\mathrm{in}}}^{E^i_{\mathrm{out}}} \frac{\mathrm{d}E}{S_{\mathrm{W}}(E)}, \tag{6}$$

where $S_{\mathrm{W}}(E)$ is the stopping power of water and $i$ refers to individual measured protons with energy $E_{\mathrm{in}}$ before the object and measured energy $E^i_{\mathrm{out}}$ beyond. Then one estimates the mean to obtain the projection value

$$p_{\gamma_n}(j\Delta\xi) = \frac{1}{N_{\gamma_n}(j\Delta\xi)} \sum_{i=1}^{N_{\gamma_n}(j\Delta\xi)} \mathrm{WEPL}_i, \tag{7}$$

where $N_{\gamma_n}(j\Delta\xi)$ is the number of protons in pixel $j\Delta\xi$ at the projection angle $\gamma_n$. At each pixel, the mean carries an intrinsic uncertainty in itself, typically expressed as the standard deviation of the mean. The variance of equation (7) is then

$$\sigma^2_{\gamma_n}(j\Delta\xi) = \frac{\sigma^2_{\mathrm{WEPL},\gamma_n}(j\Delta\xi)}{N_{\gamma_n}(j\Delta\xi)}. \tag{8}$$

The variance of the WEPL (without index $i$ since we refer to average WEPL in a projection pixel), $\sigma^2_{\mathrm{WEPL}}$, in turn depends on the uncertainty of the proton energies, which is generally attributed to energy straggling (Schulte *et al* 2005) (additional detector uncertainties will not be taken into account in this study). Therefore, the error of the exit energy propagates into the WEPL values, which is described by the error propagation formula. The first order approximation is sufficient as the second order contribution is already four orders of magnitude below the first order term. With the mean energy of the detected protons $\overline{E}_{\mathrm{out}}$, one obtains

$$\sigma^2_{\mathrm{WEPL}} = \left(\frac{\partial \mathrm{WEPL}\left(\overline{E}_{\mathrm{out}}\right)}{\partial E}\right)^2 \sigma^2_{E_{\mathrm{out}}} = \frac{\sigma^2_{E_{\mathrm{out}}}}{S^2_{\mathrm{W}}(\overline{E}_{\mathrm{out}})}. \tag{9}$$

Together with equation (8), the variance of the projection value is given by Schulte *et al* (2005)

$$\sigma^2_{\gamma_n}(j\Delta\xi) = \frac{\sigma^2_{E_{\mathrm{out}},\gamma_n}(j\Delta\xi)}{N_{\gamma_n}(j\Delta\xi)\cdot S^2_{\mathrm{W}}(\overline{E}_{\mathrm{out},\gamma_n}(j\Delta\xi))}. \tag{10}$$

### 2.2.3. 2D noise reconstruction without DDB

The basics of the noise reconstruction from the FBP for pCT were outlined by Schulte *et al* (2005) for the central pixel of pCT images, and are analogous to the x-ray CT noise reconstruction techniques shown by Huesman *et al* (1977) or Gore and Tofts (1978). Since the projection values $p_{\gamma_n}(m\Delta\xi)$ carry an error, we will treat them as random variables, with their mean and variance given by equations (7) and (10) respectively. In general, the variance of a weighted sum of random variables $X_i$ with the weights $a_i$ is

$$\mathrm{Var}\left[\sum_{i=1}^{M} a_i X_i\right] = \sum_{i,j=1}^{M} a_i a_j \,\mathrm{Cov}\left[X_i, X_j\right] = \sum_{i=1}^{M} a_i^2 \,\mathrm{Var}\left[X_i\right] + 2\sum_{i,j|i<j}^{M} a_i a_j \,\mathrm{Cov}\left[X_i, X_j\right]. \tag{11}$$

The summation over $p_{\gamma_n}(m\Delta\xi)$ in equation (4) is threefold: the sum over the angles, the projection values (convolution) and the interpolation. We use the approximation that there is no covariance among the projection values $p_{\gamma_n}(m\Delta\xi)$ since individual protons are tracked and pileup is assumed negligible.

But, due to the convolution, the filtered projections carry a mutual dependency. Each filtered projection $h_{\gamma_n}(j\Delta\xi)$ value is the linear combination of the surrounding projection values $p_{\gamma_n}(m\Delta\xi)$. As the projection values $p_{\gamma_n}(m\Delta\xi)$ are independent, we have

$$\mathrm{Cov}\left[p_{\gamma_n}(m\Delta\xi), p_{\gamma_{n'}}(m'\Delta\xi)\right] = \delta_{n,n'}\delta_{m,m'}\,\mathrm{Var}\left[p_{\gamma_n}(m\Delta\xi)\right] = \delta_{n,n'}\delta_{m,m'}\sigma^2_{\gamma_n}(m\Delta\xi), \tag{12}$$

since $\mathrm{Cov}[X,X] = \mathrm{Var}[X]$. $\delta_{ij}$ is the Kronecker delta, which is defined as

$$\delta_{ij} = \begin{cases} 0 & \text{if } i \neq j, \\ 1 & \text{if } i = j. \end{cases} \tag{13}$$

The weights from equation (11) become

$$\begin{aligned} a_i &\to \frac{\pi}{N_p}\Delta\xi \cdot g((j(\xi_n) - m)\Delta\xi)\,[1 - u(\xi_n)] \\ a_j &\to \frac{\pi}{N_p}\Delta\xi \cdot g((j(\xi_n) + 1 - m)\Delta\xi) u(\xi_n). \end{aligned} \tag{14}$$

Finally, the noise of the image can be reconstructed through

$$\mathrm{Var}\left[f(x_p,y_p)\right]=\left(\frac{\pi}{N_p}\Delta\xi\right)^2\cdot$$
$$\sum_{n=1}^{N_p}\left\{[1-u]^2\,V_{\gamma_n}(j\Delta\xi)+2\,[1-u]\,uC_{\gamma_n}(j\Delta\xi,(j+1)\Delta\xi)+u^2V_{\gamma_n}((j+1)\Delta\xi)\right\}\tag{15}$$

where $j=j(\xi_n)$ and $u=u(\xi_n)$, just as in equation (4). Following (Wunderlich and Noo 2008), we introduced the variance and covariance terms

$$V_{\gamma_n}(j\Delta\xi)=\sum_{m=-D/2}^{D/2-1}g^2((j-m)\Delta\xi)\sigma^2_{\gamma_n}(m\Delta\xi),\tag{16}$$

$$C_{\gamma_n}(j\Delta\xi,j'\Delta\xi)=\sum_{m=-D/2}^{D/2-1}g((j-m)\Delta\xi)g((j'-m)\Delta\xi)\sigma^2_{\gamma_n}(m\Delta\xi).\tag{17}$$

When summing $p_{\gamma_n}(m\Delta\xi)g((j(\xi_n)-m)\Delta\xi)\,[1-u(\xi_n)]$ and $p_{\gamma_n}(m\Delta\xi)g((j(\xi_n)+1-m)\Delta\xi)u(\xi_n)$ for interpolation, we produce two variance and two covariance terms through $\mathrm{Var}\,[a_1X+a_2X]=a_1^2\,\mathrm{Var}\,[X]+a_2^2\,\mathrm{Var}\,[X]+2a_1a_2\,\mathrm{Cov}\,[X,X]$. The $C_{\gamma_n}$ term is the covariance of the filtered projections and only the inner two sums of equation (4) bear this covariance, as we do not convolve in the angular dimension.

Wunderlich and Noo (2008) noticed that by defining

$$g_{\mathrm{C}}(j\Delta\xi)=g(j\Delta\xi)g((j+1)\Delta\xi).\tag{18}$$

Equation (17) can be written as a convolution

$$C_{\gamma_n}(j\Delta\xi,(j+1)\Delta\xi)=\sum_{m=-D/2}^{D/2-1}g_{\mathrm{C}}((j-m)\Delta\xi)\sigma^2_{\gamma_n}(m\Delta\xi).\tag{19}$$

In general, the noise reconstruction algorithm is similar to a FBP. We merely use a different prefactor, interpolation and different convolution kernels.

Furthermore, one is able to approximate the effect of the interpolation and reduce it to a single factor. A simplified variance reconstruction is then given by

$$\mathrm{Var}\left[f(x_p,y_p)\right]=f_{\mathrm{interp},\mu}\left(\frac{\pi}{N_p}\Delta\xi\right)^2\sum_{n=1}^{N_p}V_{\gamma_n}(j\Delta\xi),\tag{20}$$

where $f_{\mathrm{interp},\mu}=2/3-2/\pi^2$. In quantitative terms, the linear interpolation in combination with the Ram-Lak filter reduces the standard deviation by about 32% (more precisely: $\sqrt{2/3-2/\pi^2}\approx 0.681\,193$). See the appendix A.1 for the detailed derivation of this approximation. For our 2D noise reconstruction, including the 2D noise reconstruction using DDB, we utilize this simplification.

### 2.2.4. 2D noise reconstruction including DDB

Given the projections from a single binning depth (e.g. the rear tracker), we had to use 1D interpolation between the sampled (and convolved) data points (see equation (4)). In order to take the projections from different depths into account, a 2D interpolation is necessary. However, as the projections from two neighboring depths are hardly any different, the interpolation along $\eta$ has a negligible contribution to the variance reconstruction, if the spacing $\Delta\eta$ is sufficiently small. For the reconstruction of a 2D slice, the Radon space becomes now 3D $(\gamma,\xi,\eta)$ through the additional dimension in the $\eta$-direction: $p_{\gamma_n}(j\Delta\xi)\rightarrow p_{\gamma_n}(j\Delta\xi,k\Delta\eta)$. The DDB noise reconstruction becomes then

$$\mathrm{Var}\left[f\left(x_p,y_p\right)\right]=\left(\frac{\pi}{N_p}\Delta\xi\right)^2\cdot$$
$$\sum_{n=1}^{N_p}\left\{\,[1-u]^2\,V_{\gamma_n}(j\Delta\xi,k\Delta\eta)+2\cdot[1-u]\,uC_{\gamma_n}(j\Delta\xi,(j+1)\Delta\xi,k\Delta\eta)\right.$$
$$\left.+\,u^2V_{\gamma_n}((j+1)\Delta\xi,k\Delta\eta)\,\right\},\tag{21}$$

where $k\Delta\eta$ is closest to the corresponding binning depth (nearest neighbor interpolation). A more detailed discussion can be found in the appendix A.2. The additional simplification involving the interpolation factor $f_{\mathrm{interp},\mu}$ described at the end of section 2.2.3 (see equation (20)) can also be applied here.

### 2.3. Noise of the projections

Recall that for 2D noise reconstruction, we need to know the variance of all the projections binned at different depths, which consists of the variance of the energy, the number of protons within the pixels and the stopping power, evaluated at $\overline{E}_{\text{out}}$

$$\sigma^2_{p_{\gamma_n}}(j\Delta\xi, k\Delta\eta) = \frac{\sigma^2_{E_{\text{out}},\gamma_n}(j\Delta\xi, k\Delta\eta)}{N_{\gamma_n}(j\Delta\xi, k\Delta\eta)\cdot S^2_{\text{W}}(\overline{E}_{\text{out},\gamma_n}(j\Delta\xi, k\Delta\eta))}. \tag{22}$$

The latter is certainly the easiest to calculate, as we can use the $\overline{E}_{\text{out}}$-values straight from the scan and evaluate the stopping power of water at $\overline{E}_{\text{out}}$. The remaining two components of the variance require more detailed discussions.

In this section, we first show an analytical approach to calculate and explain the energy straggling and proton counts for *rear tracker projections* using theoretical proton energy straggling and scattering models, commonly used in the pCT reconstruction. Results from this model will be compared to the results of the MC simulation.

Since the extension of the analytical model to arbitrary distances for DDB is non-trivial, we subsequently report how the noise of *DDB projections* was calculated from the MC simulation data.

These calculations of the noise in pCT projections are an extension of Schulte *et al* (2005) work detailing the noise at the center of a cylindrical object, which will be referred to as *central pixel model*.

#### 2.3.1. Noise of rear tracker projections

*Proton counts*

For the 2D noise reconstruction, the proton counts $N$ could be taken directly from the MC simulation or scan data. However, for the proton fluence used in this work (200 protons mm$^{-2}$), the statistical fluctuation of the proton counts at the rear detector is large. This fluence corresponds to an imaging dose of about 3 mGy (Schulte *et al* 2005), which is already relatively high in the context of daily image guidance with pCT.

Accurate and smooth proton count data can be calculated through the transport theory, i.e. Fermi–Eyges theory (Fermi 1940, Eyges 1948, Gottschalk 2012). It is a bivariate Gaussian theory, which is able to predict proton MCS with sufficient accuracy. More complete models, e.g. Molière's theory (Molière 1947, Molière 1948) are not necessary, as the additional tails of the distributions, as predicted by Molière's theory, will be subject to the three standard deviations data cuts, i.e. the rejection of protons which have undergone large angle scattering or nuclear interactions (Schulte *et al* 2005). $\mathcal{F}(\xi,\theta,\eta)\mathrm{d}\xi\mathrm{d}\theta$ is the probability to find a proton within the lateral displacement $[\xi, \xi+\mathrm{d}\xi]$ and traveling along the angle $[\theta, \theta+\mathrm{d}\theta]$ at depth $\eta$, which was initially at $\xi_0 = 0$ and $\theta_0 = 0$ at depth $\eta_0 = 0$

$$\mathcal{F}(\xi,\theta,\eta)\mathrm{d}\xi\mathrm{d}\theta = \frac{1}{2\pi\sqrt{B(\eta)}}\exp\left[-\frac{1}{2}\frac{A_0(\eta)\xi^2 - 2A_1(\eta)\xi\theta + A_2(\eta)\theta^2}{B(\eta)}\right]\mathrm{d}\xi\mathrm{d}\theta, \tag{23}$$

where

$$B(\eta) = A_0(\eta)A_2(\eta) - A_1^2(\eta). \tag{24}$$

For the scattering integrals

$$A_n(\eta) = \int_0^\eta (\eta - x)^2\, T(x)\mathrm{d}x \tag{25}$$

we chose (as it is chosen in other pCT related work, e.g. Quiñones (2016) or Bopp (2014)) the scattering power proposed by Gottschalk (2010), which reads

$$T_{\text{dM}} = f_{\text{dM}}(p, v, p_1, v_1)\cdot\frac{1}{X_s}\left(\frac{E_s}{pv}\right)^2, \tag{26}$$

where $E_s = 15.0$ MeV, $X_s$ is the material dependent scattering length and

$$\begin{aligned} f_{\text{dM}} \equiv\ & 0.5244 + 0.1975\log_{10}\left[1-\left(\frac{pv}{p_1v_1}\right)^2\right] + 0.2320\log_{10}\left[\frac{pv}{\text{MeV}}\right] \\ & - 0.0098\log_{10}\left[\frac{pv}{\text{MeV}}\right]\log_{10}\left[1-\left(\frac{pv}{p_1v_1}\right)^2\right]. \end{aligned} \tag{27}$$

In order to carry out these integrals, we used the analytical expression of the cylindrical hull, but a prior reconstruction could also be used in the case of patient imaging. Our primary interest is the spatial distribution of the protons, thus we calculate $A_2(\eta)$, since

$$\langle \xi^2(\eta) \rangle = \int_{-\infty}^{\infty} \int_{-\infty}^{\infty} \xi^2 \mathcal{F}(\xi, \theta, \eta) \mathrm{d}\xi \mathrm{d}\theta = A_2(\eta). \tag{28}$$

The additional proton drift from the object edge (hull) to the tracker can be calculated using a quadratic law under the assumption that the scattering power of air is negligible (Gottschalk 2012)

$$A_2(D(\xi) + d(\xi)) = A_0(D(\xi))d^2(\xi) + 2A_1(D(\xi))d(\xi) + A_2(D(\xi)). \tag{29}$$

See figure 3 for the definition of $d(\xi)$ and $D(\xi)$.

We can apply this theory to determine the rear tracker fluence by calculating the width of the proton beam for any $\xi$. Then we superimpose the distributions, weighted by their corresponding attenuation caused by nuclear reactions, as already described by Schulte *et al* (2005). The exponential attenuation of the initial fluence $\Phi_0$ is given by

$$\Phi(\mathrm{WEPL}) = \Phi_0 \cdot e^{-N\sigma_{\mathrm{nuc}} \cdot \mathrm{WEPL}} = \Phi_0 \cdot e^{-\kappa \cdot \mathrm{WEPL}}, \tag{30}$$

where $N$ is the target (nuclei) density, $\sigma_{\mathrm{nuc}}$ is the nuclear cross section, and $\kappa = N\sigma_{\mathrm{nuc}}$ is the linear attenuation coefficient.

The attenuation coefficient can be determined by taking elastic ($\approx$80 mb) and inelastic ($\approx$270 mb) cross sections into account (values taken from Quiñones (2016) $\rightarrow$ figure 3.9 and $\rightarrow$ figure 3.12 for 'G4_O' above approximately 150 MeV; Schulte *et al* (2005) determined the attenuation coefficient, neglecting the elastic contribution, in a similar fashion) which results in an attenuation coefficient $\kappa = 0.0131\ \mathrm{cm}^{-1}$. The normalized fluence at each detector pixel is the sum of all beams that scatter into a given pixel.

*Standard deviation of the exit energy*

The determination of the standard deviation of the exit energy $\sigma_{E_{\mathrm{out}}}$ at each detector pixel is a somewhat more challenging task. Schulte *et al* (2005) suggested to calculate it from the exit energy $\overline{E}_{\mathrm{out}}$, or the WEPL value, in combination with an evaluation of Payne (1969) or Tschalär (1968a, 1968b) theories, which establish a connection between the exit energy or the WEPL to the energy straggling. However, if we want to perform 2D noise reconstruction, then Schulte's approach is not valid away from the central pixel due to the interplay of MCS and the high gradient of the object's hull along $\xi$. In the following, we will present an analytical approach, much like (Schulte *et al* 2005), which includes Tschalär's/Payne's theoretical energy straggling and also accounts for the effect of MCS. Given the proton transport and thus $A_2(\xi)$ for every exit detector pixel, that we used to determine the proton counts in section 2.3.1, we can answer the inverse question as well: Given some exit detector pixel $j\Delta\xi$, what is the distribution of initial proton positions (or initial position distribution, short IPD) on the front tracker, that scatter into $j\Delta\xi$. This process is demonstrated in figure 4. We take the distributions of the surrounding entrance pixels of $j\Delta\xi$ and calculate how much they contribute to the exit pixel sited at $j\Delta\xi$. Additionally, we weight the result with the attenuation.

We include the effect of the MCS through the IPD. Since protons from different initial positions (IP) scatter into the same pixel, they must traverse different path lengths, i.e. different parts of the objects. Therefore they lose different amounts of energy, which eventually broadens the energy spectrum. We used a straight line approximation between the entry point and the detector pixel coordinate, which may seem a poor approximation for a 25 cm diameter object. However, notice that the broadest IPD of the detector pixel at the center covers approximately only two centimeters.

Our goal is to calculate the distribution of *mean* exit energies that are collected within each detector pixel. This can be done by mapping the IPD with some function $F(j\Delta\xi, \mathrm{IP})$ to the corresponding distribution of energy losses. This function in turn can be calculated through sinogram interpolation, taken from a prior scan in combination with the straight line approximation. See the appendix A.3 for details.

Now we transform the IPDs into distributions of $\overline{E}_{\mathrm{out}}$. The transformation is given by

$$p_\mu(j\Delta\xi, \mu_n) = \sum_{x \in F^{-1}(j\Delta\xi, \mu_n)} f_{\mathrm{IP}}(x). \tag{31}$$

In general, the IPDs are closely distributed around their corresponding exit detector pixel. Despite the fact that the IPDs are the broadest at the center, the transformed distributions of mean energy losses will more closely resemble a delta distribution. Put simply, no matter where the protons that scatter into the central pixel enter the object, on average they have lost approximately the same amount of energy. On the other hand, at the object edges the energy transformation varies more rapidly. Even though the IPDs become increasingly narrow at the edges, the corresponding $\overline{E}_{\mathrm{out}}$ distribution might be broader, if the traversed thickness decreases rapidly, which is the case with the 25 cm cylinder we used. In other words, only small changes of the IP cause large changes in the average energy loss. This is due to the more rapidly changing hull and therefore more rapidly changing path lengths.

Finally, at this stage we will apply the theoretical energy straggling (see figure 5), which is governed by the differential equation of Tschalär (1968a, 1968b), here expanded up to the first order

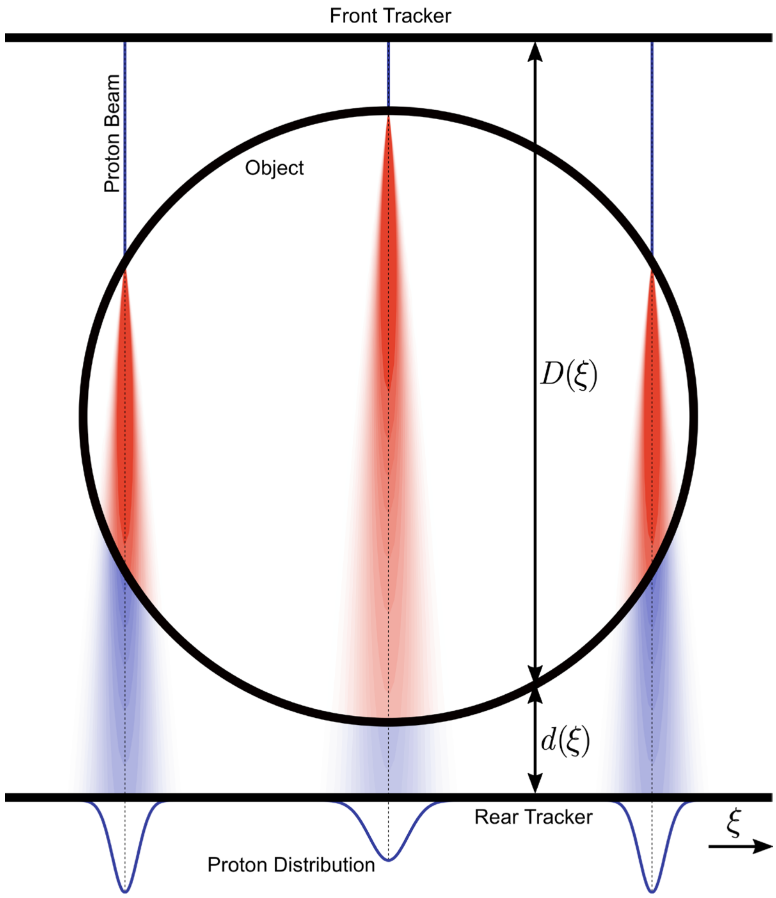


**Figure 3.** Transport theory applied to pCT. For the red colored proton beam, we have to evaluate the scattering integrals of equation (25), while for the subsequent blue colored drift through air, the quadratic law of equation (29) is sufficient. Prior to entering the object, the width of proton beam is considered infinitely small, i.e. we consider a parallel beam. Note that the scattering is exaggerated.

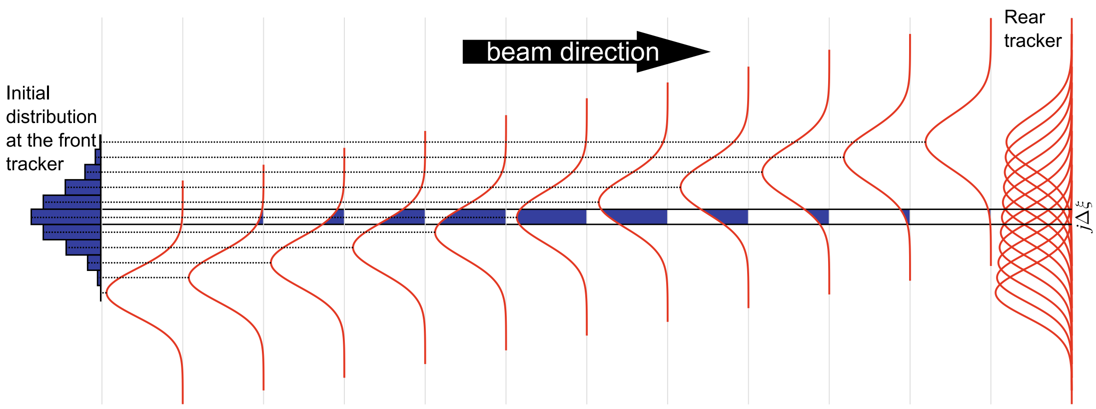


**Figure 4.** Visualization of the calculation of the initial distribution from the given proton distributions at the rear tracker. The proton distributions at the detector were spread horizontally for visual clarity. This has no geometrical meaning. We calculate the initial distribution of the pixel $j\Delta\xi$ delimited by the solid lines. The probabilities for the surrounding positions to scatter into $j\Delta\xi$ is given by the areal overlap of their distributions within $j\Delta\xi$. The corresponding probabilities are then arranged in the initial distribution along the dotted lines.

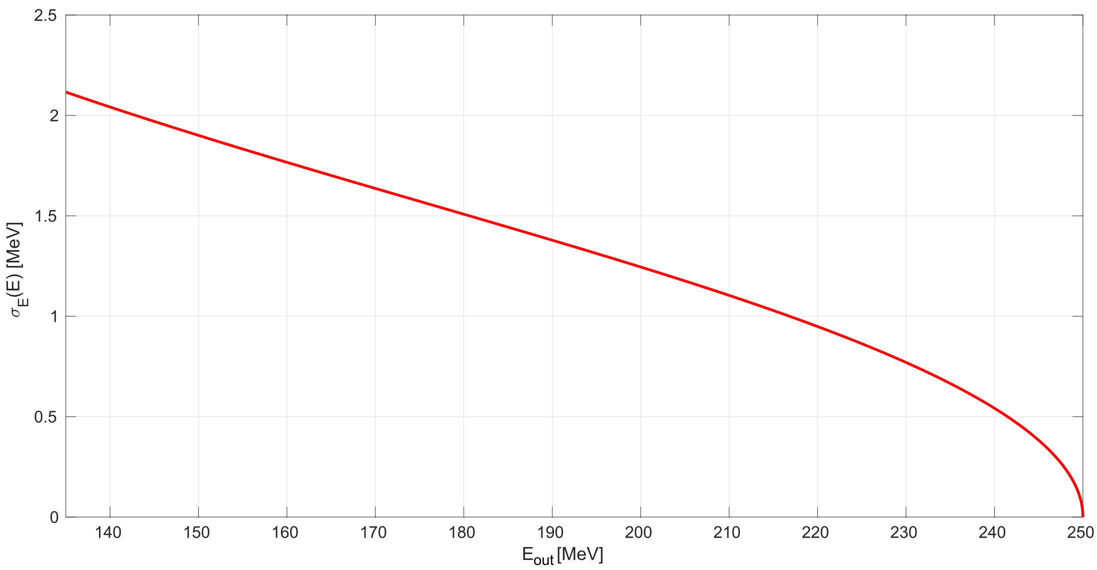


**Figure 5.** Energy straggling determined via solving the integral given in equation (34) for protons with an initial energy of $E_{\text{in}} = 250$ MeV.

$$\frac{\mathrm{d}\sigma_E^2(x)}{\mathrm{d}x} = \chi_2(E(x)) - 2\frac{\partial\chi_1(E(x))}{\partial E}\sigma_E^2(x), \tag{32}$$

where $\chi_1$ is given by the stopping power and $\chi_2$ is the straggling parameter

$$\begin{aligned}\chi_1(E) &= K_1\frac{1}{\beta^2(E)}\left[\ln\left(\frac{2mc^2\beta^2(E)}{I(1-\beta^2(E))}\right) - \beta^2(E)\right]\\ \chi_2(E) &= K_2\frac{1-\beta^2(E)/2}{1-\beta^2(E)}.\end{aligned} \tag{33}$$

For protons stopping in water, we have $K_1 \approx 170\ \text{keV cm}^{-1}$ and $K_2 \approx 0.087\ \text{MeV}^2\ \text{cm}^{-1}$. Equation (32) can be solved analytically, as outlined by Payne (1969)

$$\sigma_E^2(E) = \chi_1^2(E)\int_E^{E_{\text{in}}}\frac{\chi_2(E')}{\chi_1^3(E')}\mathrm{d}E'. \tag{34}$$

The last step involves the calculation of the standard deviation of the energy $\sigma_E$ from the distribution of mean energy losses $\overline{E}_{\text{out}}$. Each detector pixel collects protons that traversed different material thicknesses with different intensities (or normalized probabilities $p_\mu$). Thus the energy distributions at the detector pixels consist of a superposition of the individual energy spectra with their respective means $\mu_n$ and standard deviations $\sigma_n$. We can retrieve the detector distribution from the distribution of means by convolving the means distributions with the normal distribution from the energy straggling theory. Note that this is not shift-invariant convolution, as the Gaussian convolution kernel is energy dependent.

If $\mu_{\text{Det}}(j\Delta\xi)$ is the mean energy loss at each exit detector pixel $(j\Delta\xi)$, i.e. the projection value prior to the transformation into WEPL, then the variance of the energy is given by

$$\sigma_E^2(j\Delta\xi) = \sum_n p_\mu(j\Delta\xi,\mu_n)\left(\sigma_n^2 + (\mu_n - \mu_{\text{Det}}(j\Delta\xi))^2\right). \tag{35}$$

As the distribution is particularly narrow at the center of the water cylinder (all protons traversed a similar length, the diameter), the only contribution to the standard deviation comes from a single mean energy loss, which is equivalent to calculating the standard deviation solely from the straight line from the front to the rear tracker. In general, there are three opposing effects at each detector pixel, which influence each other. Firstly, the IPD, which is broad at the center and narrow at the edges. Secondly, the mean energy loss distribution, which is broad at the edges and narrow at the center. Finally, the convolution of $p_\mu$ with Gaussians according to Tschalär's theory, which has a big influence at the center (since it predicts broader Gaussian distributions at large energy losses) and a small effect at the edges, as the additional effect of energy straggling is small at small energy losses.

### 2.3.2. Noise of DDB projections

For the calculation of the noise of DDB projections at depth $\eta$ we made use of the path of every proton for which entrance and exit coordinates were recorded by the MC simulation.

The paths were reconstructed by cubic splines with adjusted velocity boundary conditions, similar to Fekete *et al* (2015), using the position and momentum direction information from the tracker planes. Li *et al* (2006) showed that the use of regular cubic splines has little effect on the spatial resolution in the pCT reconstruction, and the improved formulation by Fekete *et al* (2015) provides paths which are nearly congruent with the path determined by the original MLP formulation (Schulte *et al* 2008).

In section 2.3.1, we refer to issues with low count statistics when generating projections from the proton fluence used in our MC simulations. To circumvent this issue, a high-statistics MC dataset was generated by combining all simulated projections. This smoother dataset was used for the DDB 2D noise reconstruction by exploiting the rotational symmetry of our water cylinder, after scaling back the counts $N$ to the original fluence.

Prior to binning the data into projections, protons were selected with a three standard deviations cut on the energy and angular distributions around their mean energy and angle per projection pixel. This was done based on front tracker binning, as in the implementation of Rit *et al* (2013).

Thus for a given $\eta$, the proton tracks crossing 1 mm bins were used to calculate $\sigma^2_{p_{\gamma_n}}$ using equation (22) where $\sigma^2_{E_{\mathrm{out}},\gamma_n}$ was obtained from Gaussian fitting of the $E_{\mathrm{out}}$ distribution of the binned protons. $N_{\gamma_n}$ was simply the number of proton paths crossing the bin and $S^2_{\mathrm{W}}$ was evaluated at $\overline{E}_{\mathrm{out}}$.

### 2.4. RSP image reconstruction and noise quantification

RSP images were reconstructed for this study with an implementation of DDB FBP, using the formalism of section 2.2.1. The main principles of the algorithm are presented in Rit *et al* (2013). The path of every proton was obtained from the splines described in the previous section 2.3.2. The data cuts of section 2.3.2 were used.

The validation of the 2D noise reconstructions was performed against the noise calculated from RSP images reconstructed from the MC simulation data. Utilizing the radial symmetry of the water cylindrical phantom, annular regions of interest (ROIs) with varying radii were defined. The number of pixels in each ROI was fixed to 1000 to ensure statistical accuracy, with the radial thickness varying accordingly. The noise from the MC RSP image at a given radius was defined as the standard deviation of the distribution of RSP values within a ROI. The standard deviation was calculated from a Gaussian fit in each RSP distribution. For the central pixel and improved models, the noise determination as a function of the distance from the center of the object was calculated by means of a line profile across a diameter on the 2D noise reconstruction. The pixel grid used for all image reconstructions shown was $280\ \mathrm{mm} \times 280\ \mathrm{mm}$ with $1\ \mathrm{mm} \times 1\ \mathrm{mm}$ pixels.

Ideal WEPL projections for parallel rays, calculated analytically for the water cylinder, were discretized on the same grid as the rear-tracker or DDB binned projections. These were used to reconstruct RSP images as described above. We used these images to evaluate the impact of partial volume effects (for example at the object's edge) and reconstruction from discretized projections on the standard deviation calculated with the annular ROIs. This was done by calculating the standard deviation analytically instead of using Gaussian fits.

## 3. Results

Equation (22) gives $\sigma^2_{\mathrm{WEPL}}$ of a projection as a function of $S_{\mathrm{W}}$, $\sigma_{E_{\mathrm{out}}}$ and $N$ within the pixels. In figure 6, each of the aforementioned components is shown along the lateral coordinate, for the MC data, the central pixel model and the improved model taking into account the effect of MCS. The three curves for $S_{\mathrm{W}}$ and $N$ were nearly indistinguishable, while for $\sigma_{E_{\mathrm{out}}}$ and $\sigma^2_{\mathrm{WEPL}}$ good agreement between the MC data and the improved rear tracker model accounting for MCS was observed. The largest $\sigma_{\mathrm{WEPL}}$ error between the MC data and the improved model was about 8% at $\xi = 100\ \mathrm{mm}$. The central pixel model, which ignores MCS, failed to correctly predict $\sigma_{E_{\mathrm{out}}}$ and $\sigma^2_{\mathrm{WEPL}}$ away from the object's center.

Figure 7 shows the effect of the binning location on $\sigma_{\mathrm{WEPL}}$. The distance is measured from the front tracker ($\eta = 0$). Binning at the rear tracker ($\eta = 260\ \mathrm{mm}$) results in high noise at the edges of the object (equivalent to the MC data $\sigma_{\mathrm{WEPL}}$ of figure 6). We observed that the increase of $\sigma_{\mathrm{WEPL}}$ with $\xi$ approaching the object's edge was most pronounced at the rear tracker, and that this effect gradually disappeared as $\eta$ approached 0 near the front tracker.

Figure 8 presents a 2D noise reconstruction obtained using either noise projections obtained by binning the protons at the rear tracker (equation (15)) or with DDB (equation (21)). The effect on the noise image of the 'interference' between the 2D image pixel grid and the 1D projection grid, as well as that of using a constant term for the linear interpolation as explained in section 2.2.3, are shown. Generally, with rear tracker binning, the noise increased towards the object's edge, while for DDB it appeared constant with a slight decrease at the edge. High noise was observed at the object's boundary.

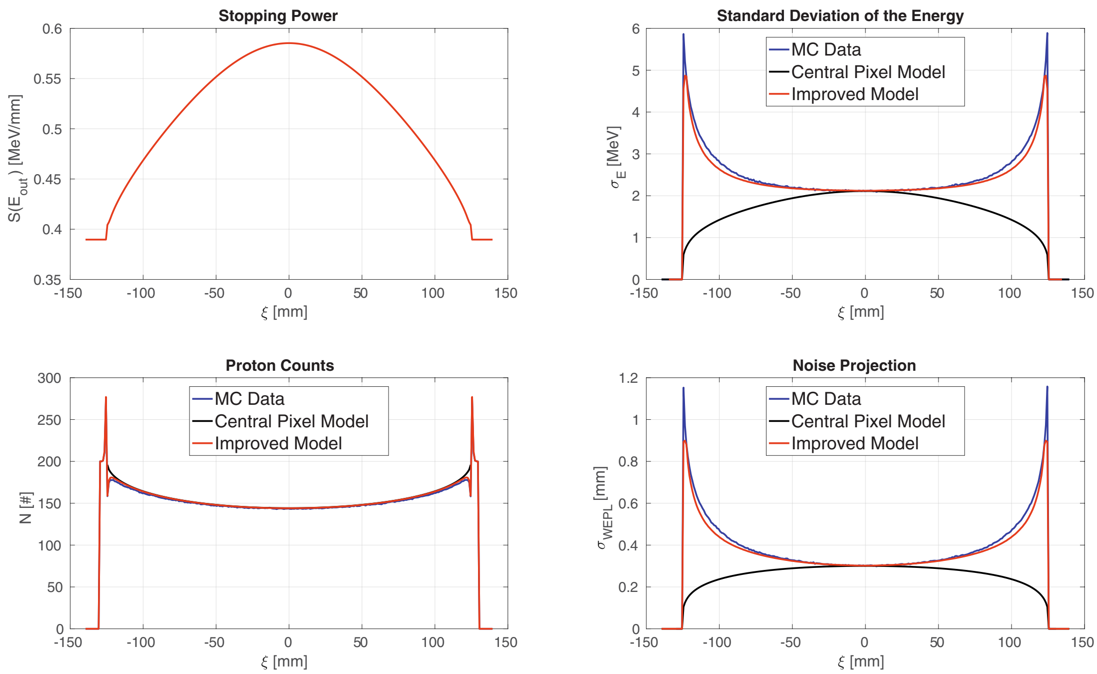


**Figure 6.** Results from rear tracker binning ($\eta = 260$ mm) for a single projection as profiles along the lateral coordinate $\xi$ for the components of equation (22) for the central pixel model, the improved model and MC data. The stopping power evaluated at the mean exit energy (upper left) is shown only for the MC data, as the three curves overlapped. Data from high statistics MC simulations were used.

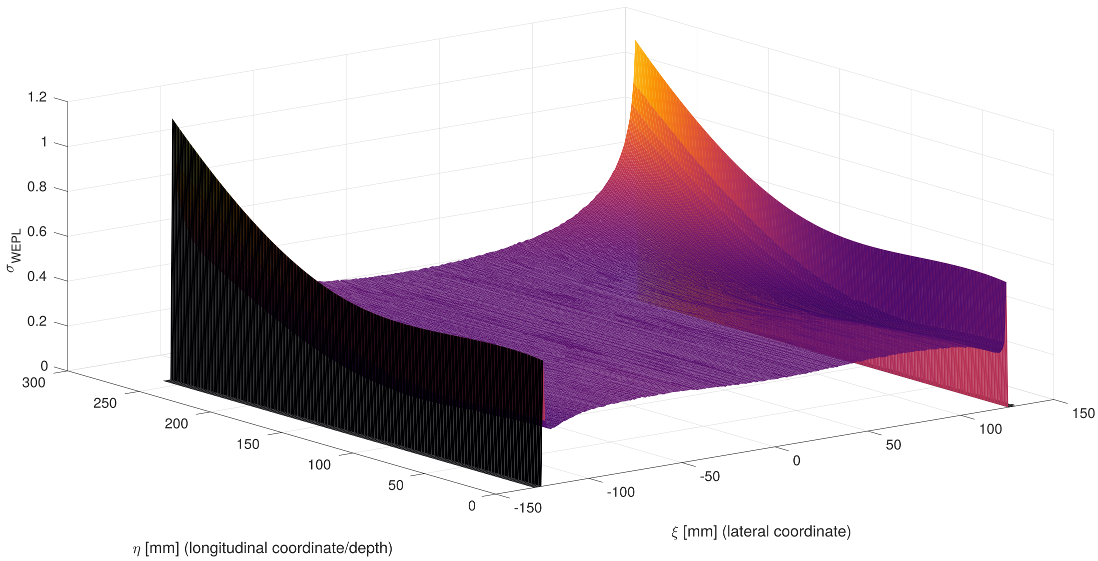


**Figure 7.** Noise projection profiles along the lateral coordinate $\xi$, shown as a function of the longitudinal coordinate of the binning position $\eta$. $\eta = 0$ corresponds to a binning at the front tracker, while $\eta = 260$ mm at the rear tracker. Data from high statistics MC simulations were used.

Finally, in figure 9, profiles through the 2D noise reconstructions based on the central pixel model, the improved model for rear tracker binning and DDB (in this case direct use of MC data, see section 2.3.2) are compared to that obtained from the MC reconstructed RSP image (using annular ROIs), as a function of the radius from the center of the object. For indicative purposes, the standard deviation for the RSP image from discretized ideal projections is also shown. We observed that the improved model and MC data-based DDB accurately reproduced the behavior of the noise observed in the reconstructed RSP images. When using rear tracker binning, an increase of 60% in image noise was observed at the edge of the 12.5 cm radius object when compared to its center. This effect was poorly captured by the central pixel model, which underestimated noise by up to 40% in this case. Interestingly, DDB negated the radial noise increase observed with rear tracker binning, producing generally lower noise values which decreased less than 5% with radius. The ideal projections yielded large standard deviations at the object's edge which corresponded to the spikes observed in the noise from the annular ROIs.

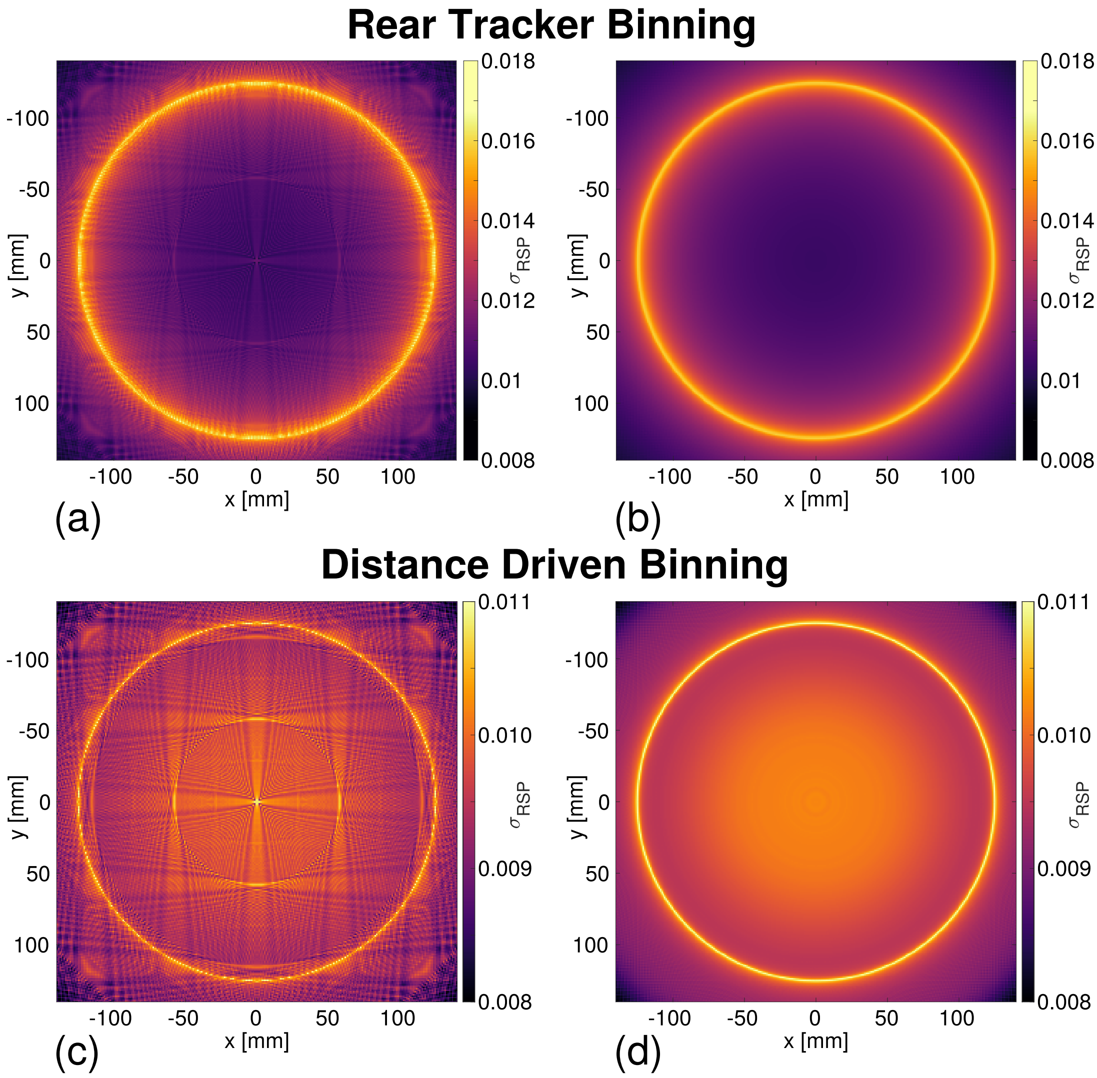


**Figure 8.** Noise images reconstructed without DDB ((a) and (b)) and with DDB ((c) and (d)). The left column ((a) and (c)) shows the effect of 'interference' between the 2D image pixel grid and the 1D projection grid. The right column ((b) and (d)) shows the smoothed versions reconstructed by using a constant term for the linear interpolation. The results from rear tracker binning were obtained from the improved model while for the DDB directly from high statistics MC data. Notice the different scales.

## 4. Discussion

In this study, we presented a formalism for 2D noise reconstruction in pCT based on a beam of incident protons traveling in parallel. 2D noise reconstructions of a cylindrical water phantom were obtained from variance projections (equation (22)) using an FBP algorithm, either for rear tracker binning or DDB.

For projection noise, results from MC simulation data, a central pixel model and an improved model were shown for rear tracker binning (see figure 6). Good agreement was obtained for rear tracker binning when using the improved model and the MC data. We made use of the improved analytical model, in addition to MC simulations, to better isolate the contributions to projection noise and help explain the shortcomings of the central pixel model, which were not readily deduced from MC data. As a side note, the central pixel and improved models yielded smoother variance projections and noise images as they do not suffer from statistical fluctuations as MC does, while being less demanding on computing resources. This may increase convergence speeds when optimizing fluence patterns for FMpCT.

An important finding of this work is the influence of MCS on the calculation of the variance projections. As shown in figure 6, the result of the calculation of the variance projection using the central pixel model, which neglects the effect of MCS, deviates considerably from the results obtained with MC. The deviation mainly stems from the estimation of the variance of the energy in a pixel. Even for a mono-energetic proton beam, there are two main contributions to the variance of the energy. The first is the proton energy straggling. It is the dominant contribution at the center of the object and as it is accounted for in the central pixel model, both analytical models (central pixel and improved) and MC yield very similar results for the variance projections in this region

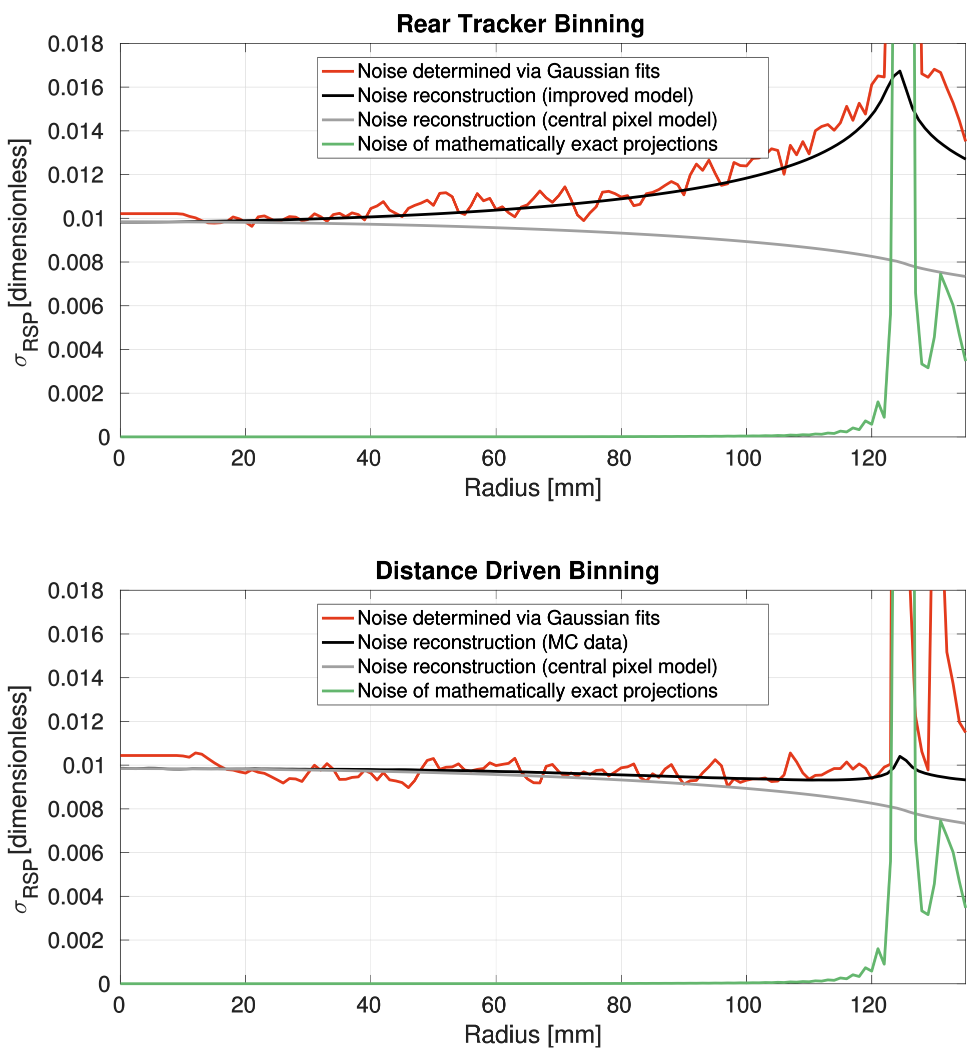


**Figure 9.** Noise profile comparison, as a function of the radius, between MC, the central pixel model, the improved model and exact mathematical projections, for rear tracker binning (upper) and distance driven binning (lower) reconstructions. The noise from the MC and from the exact mathematical projections RSP image is obtained from the annular ROIs. The noise of the central pixel model and improved model are obtained from a line profile along the diameter of the reconstructed noise map (with the simplified interpolation effect, i.e. figures 8(b) and (d)).

of the phantom. The second contribution to the variance of the energy comes from MCS. Protons can scatter in a pixel having traversed very different paths. This leads to an increase of the variance of the energy beyond the level expected from energy straggling of protons which follow very similar paths and cannot be described by the central pixel model. The improved model takes this effect into account and therefore reaches very good agreement with the MC. Nevertheless, the results shown in this study refer to a homogeneous cylindrical phantom. (Homogeneous water is yet a typical assumption for the MLP, especially if no prior image is available.) The impact of heterogeneities as well as more complex phantom surfaces will have to be incorporated to the improved model.

As shown in figure 7, the shape of the noise projection profiles along the lateral coordinate $\xi$ changes when binning protons at different depths along the longitudinal coordinate $\eta$. The noise projection is described by higher noise at the edges of the object. For rear tracker binning ($\eta = 260$ mm), this effect is very pronounced due to the importance of drift along the increasing air gap between the object and the rear tracker which causes protons with widely different paths to reach the same projection pixel. DDB mitigates this for projections with $\eta$ in the object by using the MLP. This can also be appreciated in figure 9 where we observed that the image noise from DDB is about 80% lower at 100 mm radius than for rear tracker binning, and more interestingly, relatively flat versus the object's radius.

Good agreement between the results from our noise reconstruction formalism and noise analysis using annular ROIs on the reconstructed image was observed. Slight deviations at the object's edge could be attributed to effects present in the reconstruction of discretized ideal projections (see figure 9). In order to reduce the computational time needed, we exploited the radial symmetry of the phantom and the resulting radial symmetry of the reconstructed noise map and therefore used annular ROIs for the quantification of the noise from the MC. This assumes that there is no correlation between the different pixels, which is not entirely true (Wunderlich and

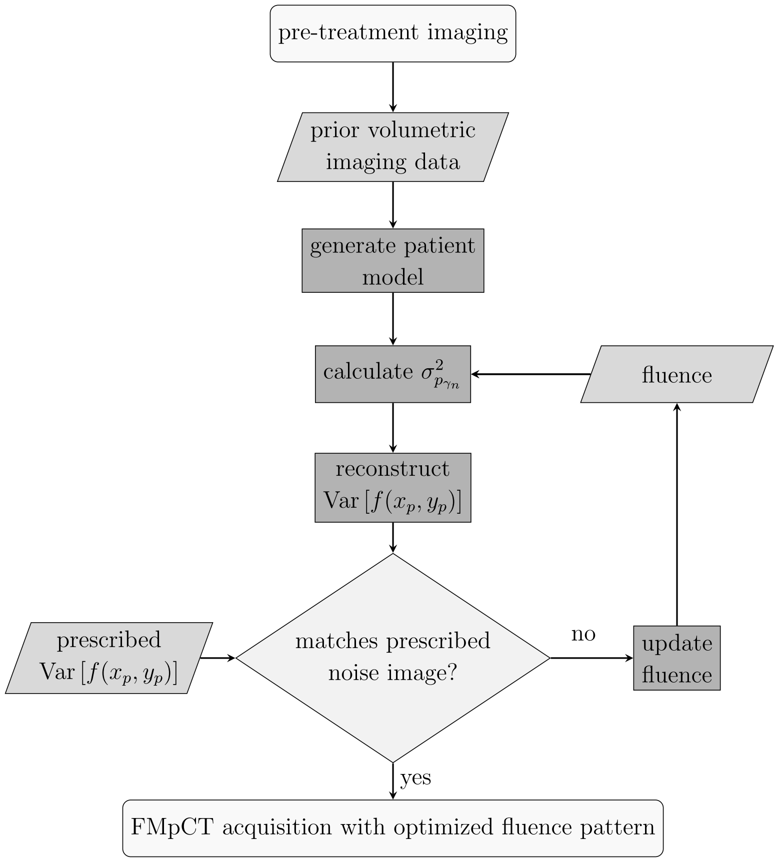


**Figure 10.** Flowchart illustrating how a fluence pattern would be optimized on the basis of the noise reconstruction formalism presented in this work.

Noo 2008). A noise quantification from MC that would bypass this assumption would be done pixel-wise on a large set of different RSP images. In that case, the noise in every pixel would be the standard deviation of the RSP values of that pixel from all RSP image realizations.

Note that any analytical noise reconstruction depends on the choice of the convolution kernel. It has a significant impact on the noise, via the corresponding frequency windowing. Alternatives include the Shepp–Logan or the Hanning convolution kernels, which show greater noise suppression and reduction of ringing artifact (Buzug 2008a). In the present work, we chose the Ram-Lak kernel, given in equation (3) or shown in figure A1. Its alternating side-lobes cancel one another in the expression of the convolution kernel, which results in minimal correlation (only nearest neighbors contribute to the covariance) as discussed in appendix A.1. The general pCT noise reconstruction with an arbitrary filter is given by equation (21), where different expressions for $g\,(j\Delta\xi)$ can be implemented in equations (16) and (17).

How different convolution kernels affect the noise in the reconstructed image has been investigated before by, for example, Zhang and Ning (2008) for x-ray cone-beam CT. Here it is shown that different filters cause an approximate (multiplicative) global shift on the overall noise distribution. Similar behavior can be expected for the pCT noise reconstruction.

In addition to the intrinsic physical effects mentioned above, real detector performance will also affect the noise in a pCT image. In reality, the energy of every proton can be measured with finite accuracy. This will be manifested as increased variance of the energy. Bashkirov *et al* (2016) reported that for their pCT setup, the energy detector uncertainty was 3 mm water equivalent path length for any given object's water equivalent thickness. Similarly, the tracking system position resolution will impact the estimation of the proton trajectory, which in turn will magnify the MSC effect on the final noise image. Finally, other detector limitations such as pile-up and non-uniform detector performance could alter the noise image with respect to what is reconstructed assuming that every proton that exits the object can be detected with the same accuracy. Further work will aim at carefully investigating the impact of detector uncertainties by making use of the validated simulation platform of Giacometti *et al* (2017) as well as experimentally acquired pencil beam scanning data from Dedes *et al* (2018).

The formalism for 2D noise reconstruction we presented was developed for FMpCT; figure 10 illustrates how a clinical implementation would rely on prior imaging data to generate a patient model used for calculating $\sigma^2_{p_{\gamma_n}}$ as input to noise reconstruction. $\sigma^2_{p_{\gamma_n}}$ would be calculated on the basis of an extension of the improved model we presented, or using MC simulation to fully account for heterogeneities in the patient. By comparing the noise reconstruction for a given fluence to a prescribed Var $[f(x_p, y_p)]$, the fluence may be optimized in an iterative procedure, as in Bartolac *et al* (2011). The patient model may be generated on the basis of an existing diagnostic CT scan, a previous full fluence pCT scan or even a pseudo-CT generated from a magnetic resonance imaging scan (Rank *et al* 2013, Koivula *et al* 2016, Maspero *et al* 2017). In addition to incorporating a realistic detector model, future work will also establish the FMpCT fluence optimization strategy, the development of the corresponding PBS modulation as well as the validation of noise reconstruction using experimental data.

## 5. Conclusion

In this paper, we developed a 2D image noise reconstruction formalism to account for both rear tracker binning and DDB in pCT in homogeneous media, assuming parallel proton beams for eventual use in FMpCT fluence optimization. We obtained good agreement between our formalism and with noise estimated from reconstructed images using annular ROIs. The use of DDB slightly decreased the image noise when compared to rear tracker binning and yielded more uniform noise throughout the image. MCS should not be neglected when predicting image noise for pixels away from the center of an object in a pCT scan.

## Acknowledgments

This work was supported by the German Research Foundation (DFG) project #388731804 'Fluence modulated proton computed tomography: a new approach for low-dose image guidance in particle therapy' and the DFG's Cluster of Excellence Munich-Centre for Advanced Photonics (MAP), by the Bavaria-California Technology Center (BaCaTeC) and by the Bavaria-France Cooperation Centre (BFHZ). David Hansen and Chiara Gianoli are acknowledged for fruitful discussions. We thank Jannis Dickmann for help at the proofreading stage as well as Marco Riboldi for his support of this work.

## Appendix

### A.1. Approximate variance reconstruction

In this section, we describe how equation (15) can be approximated through equation (20). Consider the two convolution kernels $g^2(j\Delta\xi)$ (equation (3)) and $g_C(j\Delta\xi)$ (equation (18)) (shown in figure A1) of the convolutions necessary for the reconstruction of the variance in $V_{\gamma_n}$ (equation (16)) and $C_{\gamma_n}$ (equation (19)) respectively. With the Ram-Lak filter, $g_C(j\Delta\xi)$ takes an especially simple form. Due to the alternating structure of $g(j\Delta\xi)$, a shift by $1\Delta\xi$ cancels all side lobes. Only adjacent pixels mutually influence each other (different apodization windows may have more complex convolution kernels).

In figure A1, one can see that $g^2(j\Delta\xi)$ and $g_C(j\Delta\xi)$ have both very limited reach. As a consequence, each filtered projection value is approximately only a weighted sum of its nearest neighbors (for the Ram-Lak covariance kernel, it is exactly only one nearest neighbor). Under the assumption that the projections are locally approximately constant, we are able to approximate all projection values (noise values) with the one at the center of the convolution kernel

$$V_{\gamma_n}(j\Delta\xi) \approx \sigma^2_{\gamma_n}(j\Delta\xi) \sum_{m=-D/2}^{D/2-1} g^2(m\Delta\xi) \tag{A.1}$$

$$C_{\gamma_n}(j\Delta\xi, (j+1)\Delta\xi) \approx \sigma^2_{\gamma_n}(j\Delta\xi) \sum_{m=-D/2}^{D/2-1} g_C(m\Delta\xi). \tag{A.2}$$

As the sum of equation (A.1) converges quickly, we can extend it to infinity. Thus, with the expression of the Ram-Lak filter (equation (3)), one is able to evaluate the sum analytically by applying Parseval's identity to the corresponding Fourier expansion components (as explained in any book on Fourier calculus)

$$\begin{aligned}\sum_{m=-D/2}^{D/2-1} g^2(m\Delta\xi) &\approx \sum_{m=-\infty}^{\infty} g^2(m\Delta\xi) \\ &\overset{\text{equation (3)}}{=} \frac{1}{(2\Delta\xi)^4} + \frac{2}{(\pi\Delta\xi)^4} \cdot \underbrace{\sum_{m=1}^{\infty} \frac{1}{(2m-1)^4}}_{\pi^4/96} = \frac{1}{12(\Delta\xi)^4}.\end{aligned} \tag{A.3}$$

With the Ram-Lak filter, the sum in equation (A.2) has only two (equal) terms (see figure A1)

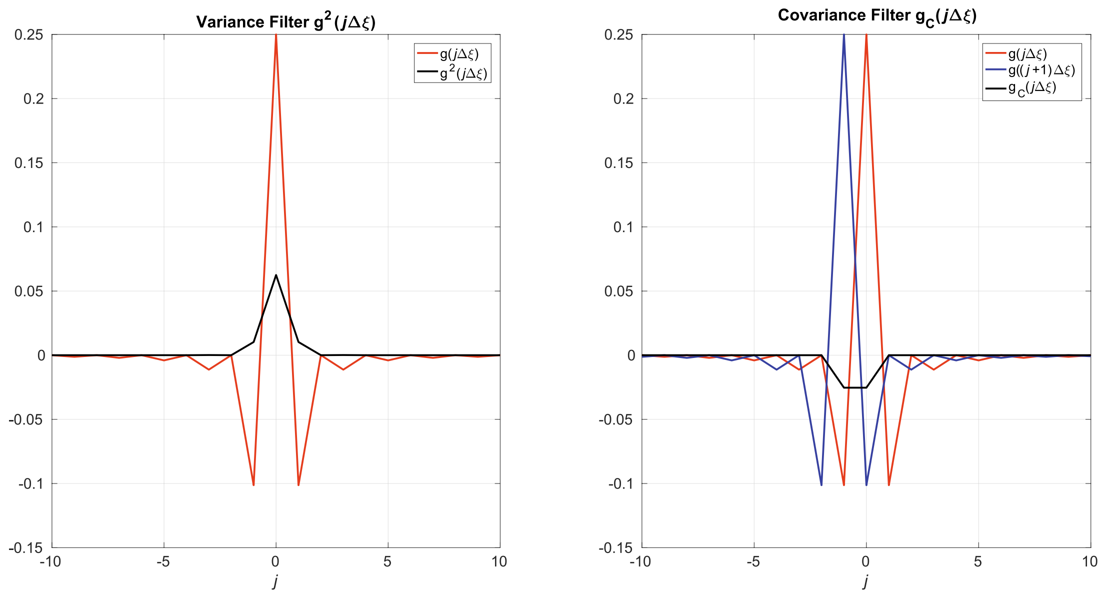


**Figure A1.** Variance and covariance filters (black lines) for unit detector spacing $\Delta\xi = 1$.

$$\sum_{m=-D/2}^{D/2-1} g_C(m\Delta\xi) \overset{\text{equations (18) and (3)}}{=} -\frac{1}{2\pi^2(\Delta\xi)^4}. \tag{A.4}$$

Finally, we can factorize equation (15):

$$\text{Var}\left[f(x_p, y_p)\right] = \left(\frac{\pi}{N_p}\Delta\xi\right)^2 \sum_{n=1}^{N_p} \frac{\sigma^2_{\gamma_n}(j\Delta\xi)}{12(\Delta\xi)^4} \left\{(1-u)^2 + 2(1-u)u\frac{-12}{2\pi^2} + u^2\right\}. \tag{A.5}$$

The factorized term is the approximation of the convolution, given by equation (A.1), while the term in curly brackets comprises the interpolation effect on the noise. The reconstruction in terms of the interpolation effect is then given through

$$\text{Var}\left[f(x_p, y_p)\right] = \left(\frac{\pi}{N_p}\Delta\xi\right)^2 \sum_{n=1}^{N_p} V_{\gamma_n}(j\Delta\xi) f_{\text{interp}}(u), \tag{A.6}$$

where

$$f_{\text{interp}}(u) = (1-u)^2 + 2(1-u)u\frac{-12}{2\pi^2} + u^2. \tag{A.7}$$

Since there is no preferred query point for the interpolation, we assume $u$ to be uniformly distributed in [0, 1], therefore $f_{\text{interp}}$ can be approximated by its mean

$$f_{\text{interp},\mu} = \int_0^1 f_{\text{interp}}(u)\text{d}u = \frac{2}{3} - \frac{2}{\pi^2}. \tag{A.8}$$

Replacing $f_{\text{interp}}(u)$ by $f_{\text{interp},\mu}$ in equation (A.6) yields the expression given in equation (20).

In reality, the distribution of $u$-values is not perfectly uniform. Figure A2 shows the mean of equation (A.7) for a finite set of projections. The resulting structures in figure A2 are caused by the 'interference' between the 2D image pixel grid and the 1D projections grid. It is an inherent property of accurate noise reconstruction, which eventually superimposes with the noise projections.

### A.2. 2D noise reconstruction including DDB

Here we will present a more thorough discussion of the 2D interpolation involved in the DDB variance reconstruction, as mentioned in section 2.2.4. We will discuss the effect of this 2D interpolation on the pCT noise based on bilinear interpolation (see figure A3). With the bilinear interpolation, the reconstruction becomes

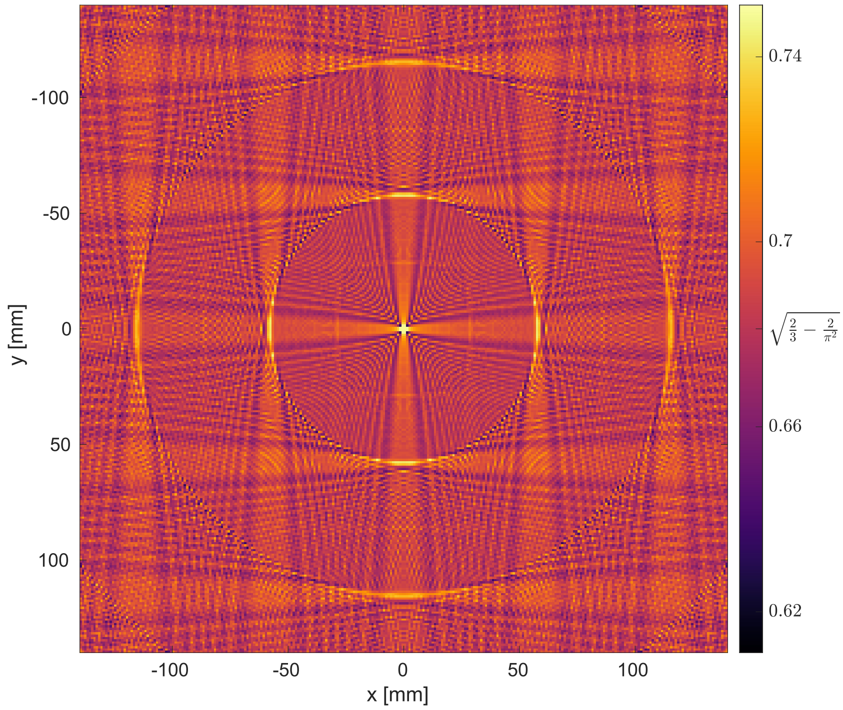


**Figure A2.** Exact noise reduction per pixel for an image, reconstructed with linear interpolation and the Ram-Lak filter. The image measures 280 mm $\times$ 280 mm with 1 mm $\times$ 1 mm voxel size. The structures are a consequence of the interference with the 1 mm spaced projections. Notice that the center is particularly high, as its pixel center is for most angles close to a sampled projection value and thus profits from the interpolation less. Pixels with higher values happen to fall on the discrete projection values more often than in between. Deviations from the approximation are, however, in general quite small.

$$\begin{aligned} f(x_p, y_p) = \frac{\pi}{N_p}\Delta\xi \sum_{n=1}^{N_p} \sum_{m=-D/2}^{D/2-1} & p_{\gamma_n}(m\Delta\xi, k\Delta\eta) g((j-m)\Delta\xi)\,[1-u]\,[1-v] \\ & + p_{\gamma_n}(m\Delta\xi, k\Delta\eta) g((j+1-m)\Delta\xi) u\,[1-v] \\ & + p_{\gamma_n}(m\Delta\xi, (k+1)\Delta\eta) g((j-m)\Delta\xi)\,[1-u]\,v \\ & + p_{\gamma_n}(m\Delta\xi, (k+1)\Delta\eta) g((j+1-m)\Delta\xi) uv, \end{aligned} \tag{A.9}$$

where

$$v = v(\eta_n) = \frac{\eta_n - k\Delta\eta}{\Delta\eta}, \tag{A.10}$$

and $\eta_n = \eta_n(x_p, y_p) = -x_p \sin(\gamma_n) + y_p \cos(\gamma_n)$. Just as in equation (15), the dependencies $j = j(\xi_n)$ and $k = k(\eta_n)$ are implicit.

Just as we had before, projection values from different angles $\gamma_n$ as well as along the $\xi$-coordinate $m\Delta\xi$ are independent. However, this holds only true for $m\Delta\xi$-values binned at the same depth $\eta$. Since, due to the bilinear interpolation, we sum up projection values from different depths, we have to take their covariance into account.

$$\begin{aligned} \mathrm{Cov}\left[p_{\gamma_n}(m\Delta\xi, k\Delta\eta), p_{\gamma_{n'}}(m'\Delta\xi, k'\Delta\eta)\right] &= \delta_{n,n'}\delta_{m,m'}\mathrm{Cov}\left[p_{\gamma_n}(m\Delta\xi, k\Delta\eta), p_{\gamma_n}(m\Delta\xi, k'\Delta\eta)\right] \\ &\equiv \delta_{n,n'}\delta_{m,m'} C_{\gamma_n}(m\Delta\xi, k\Delta\eta, k'\Delta\eta). \end{aligned} \tag{A.11}$$

Without further specifying this covariance term and following the procedure from above (equations (11), (14) and (15)), the variance of equation (A.9) becomes

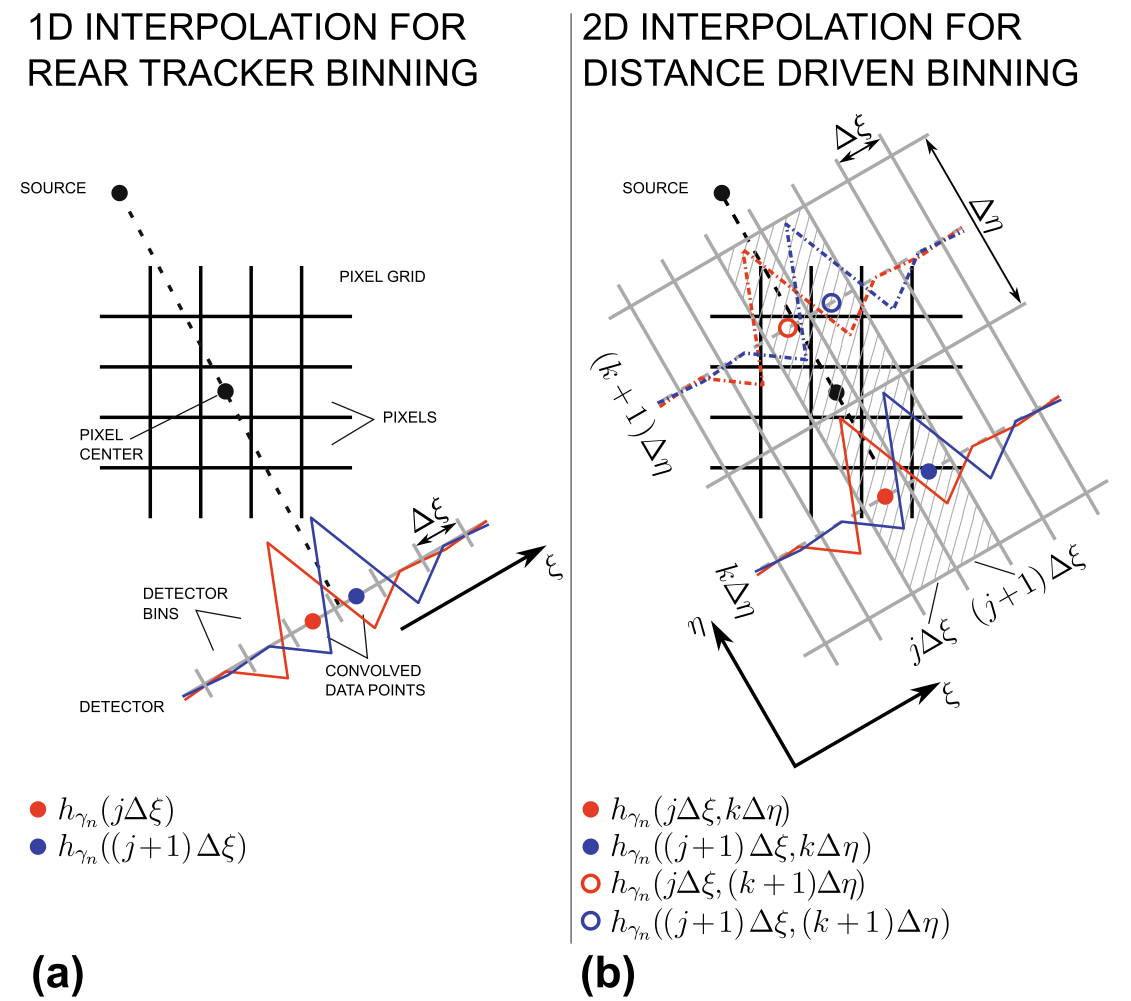


**Figure A3.** Interpolation for a 2D image reconstruction (a) without and (b) with DDB. (a) For binning at the rear tracker, the value at the pixel center (black dot) requires a 1D interpolation (at the dashed line) of the convolved projection values (red and blue dot), which are a weighted linear combination of all projection values and thus mutually dependent due to the prior convolution with the convolution kernels (red and blue zigzag lines), as shown in figure A1. (b) In the DDB case, a 2D interpolation is necessary, where projections, binned at different depths (i.e. $k\Delta\eta$ and $(k+1)\Delta\eta$), are involved. The four hatched pixels contribute to the value at the pixel center (black dot). The convolution is still only along $\xi$. The detector spacing $\Delta\xi$ and the depth spacing $\Delta\eta$ are only drawn different for visual clarity.

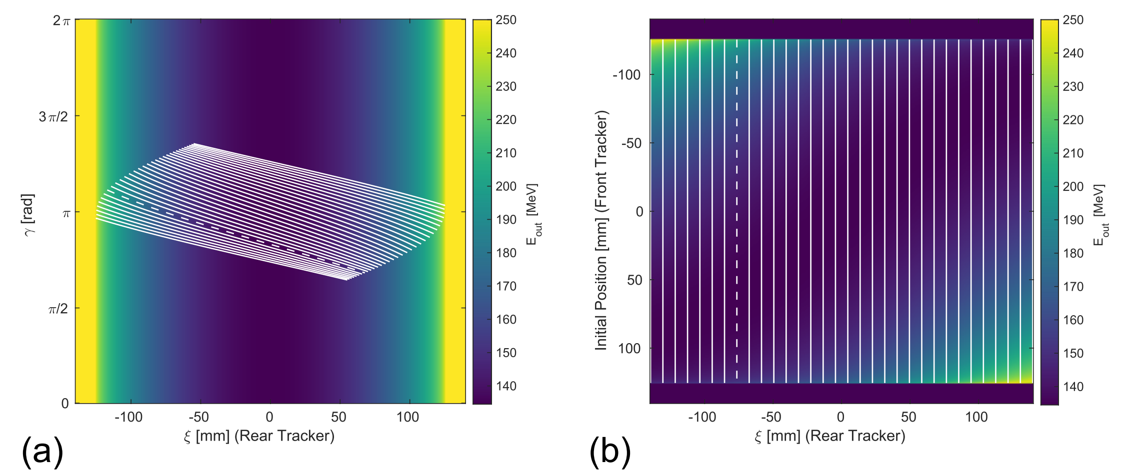


**Figure A4.** Mapping of the Radon space in units of the exit energy (a) to $F(j\Delta\xi, \mathrm{IP})$ (b). The data on the white lines in (b) was interpolated from the data shown in (a) along the corresponding curved lines, where the dashed lines in both figures belong together and are supposed to give orientation.

$$\begin{aligned}\mathrm{Var}\left[f\left(x_p,y_p\right)\right]=\left(\frac{\pi}{N_p}\Delta\xi\right)^2\sum_{n=1}^{N_p}\Big\{&[1-u]^2[1-v]^2V_{\gamma_n}(j\Delta\xi,k\Delta\eta)+u^2[1-v]^2V_{\gamma_n}((j+1)\Delta\xi,k\Delta\eta)\\&+[1-u]^2v^2V_{\gamma_n}(j\Delta\xi,(k+1)\Delta\eta)+u^2v^2V_{\gamma_n}((j+1)\Delta\xi,(k+1)\Delta\eta)\\&+2\cdot[1-u]u[1-v]^2C_{\gamma_n}(j\Delta\xi,(j+1)\Delta\xi,k\Delta\eta,k\Delta\eta)\\&+2\cdot[1-u]^2[1-v]vC_{\gamma_n}(j\Delta\xi,j\Delta\xi,k\Delta\eta,(k+1)\Delta\eta)\\&+2\cdot[1-u]u[1-v]vC_{\gamma_n}(j\Delta\xi,(j+1)\Delta\xi,k\Delta\eta,(k+1)\Delta\eta)\\&+2\cdot[1-u]u[1-v]vC_{\gamma_n}((j+1)\Delta\xi,j\Delta\xi,k\Delta\eta,(k+1)\Delta\eta)\\&+2\cdot u^2[1-v]vC_{\gamma_n}((j+1)\Delta\xi,(j+1)\Delta\xi,k\Delta\eta,(k+1)\Delta\eta)\\&+2\cdot[1-u]uv^2C_{\gamma_n}(j\Delta\xi,(j+1)\Delta\xi,(k+1)\Delta\eta,(k+1)\Delta\eta)\Big\},\end{aligned}\tag{A.12}$$

where the equivalent expressions of $V_{\gamma_n}$ and $C_{\gamma_n}$ in two dimensions are

$$V_{\gamma_n}(j\Delta\xi,k\Delta\eta)=\sum_{m=-D/2}^{D/2-1}g^2((j-m)\Delta\xi)\sigma^2_{\gamma_n}(m\Delta\xi,k\Delta\eta),\tag{A.13}$$

$$\begin{aligned}&C_{\gamma_n}(j\Delta\xi,j'\Delta\xi,k\Delta\eta,k'\Delta\eta)\\&\quad=\sum_{m=-D/2}^{D/2-1}g((j-m)\Delta\xi)g((j'-m)\Delta\xi)C_{\gamma_n}(m\Delta\xi,k\Delta\eta,k'\Delta\eta).\end{aligned}\tag{A.14}$$

The covariance values between two data points from the same depth ($k=k'$) becomes again $C_{\gamma_n}(m\Delta\xi,k\Delta\eta,k\Delta\eta)=\sigma^2_{\gamma_n}(m\Delta\xi,k\Delta\eta)$, just like in equation (12). The remaining covariances are between projection values from adjacent depths, which we have not yet discussed. Note that projection values $p_{\gamma_n}(m\Delta\xi,k\Delta\eta)$ and $p_{\gamma_n}(m\Delta\xi,(k+1)\Delta\eta)$ are calculated from almost the same data set of protons, given that the pixel spacing in the $\eta$-direction ($\Delta\eta$) is sufficiently small. This is due to that fact that within $[k\Delta\eta,(k+1)\Delta\eta]$ only very few protons outside of $m\Delta\xi$ will scatter laterally into $m\Delta\xi$ and at the same time only very few protons within $m\Delta\xi$ will scatter to neighboring pixels. Thus projection values from any two neighboring depths are hardly different (below approximately 0.2 mm WEPL for the reconstruction of our simulation (see section 2.1), using $\Delta\eta=1$ mm) and can therefore be considered equal. We can thus assume that depth adjacent projection values are perfectly correlated while the two diagonal pixels in the bilinear interpolation have no correlation

$$C_{\gamma_n}(m\Delta\xi,k\Delta\eta,k'\Delta\eta)=\delta_{k,k'}\sigma^2_{\gamma_n}(m\Delta\xi,k\Delta\eta).\tag{A.15}$$

As there is now no difference between the projection values at $k\Delta\eta$ and $(k+1)\Delta\eta$, we can now make the replacement

$$C_{\gamma_n}(j\Delta\xi,j'\Delta\xi,k\Delta\eta,k'\Delta\eta)\rightarrow C_{\gamma_n}(j\Delta\xi,j'\Delta\xi,k\Delta\eta).\tag{A.16}$$

The noise reconstruction including DDB is then given by the expression of equation (21). It is similar to the noise reconstruction of the rear tracker binning (equation (15)), as we neglected the covariance along $\eta$. The $v$-dependence in equation (A.12) cancels under the approximation of equation (A.16). The index $k=k(\eta_n)$ is still query point dependent, but as the projection values of two neighboring depths are considered to be equal, nearest neighbor or linear interpolation along $\eta$ is sufficient for the noise map reconstruction.

### A.3. Sinogram interpolation

We can estimate the function $F(\xi,\mathrm{IP})$ that maps the IPs to the corresponding energy loss along the straight line from the IP-hull intersection to some exit detector pixel $j\Delta\xi$ by interpolating across the Radon space, as the various straight proton paths, that contribute to one pixel, are line integrals from neighboring projections coming from different angles $\gamma_n$. The set of angles results from the IP-hull intersection coordinate (i.e. projecting the IPs onto the hull) and the exit detector pixel coordinate. Therefore every IP determines an angle $\gamma_{\mathrm{IP}}(j\Delta\xi)$, which is different for every $j\Delta\xi$. The set of the corresponding $\xi$ values in the Radon space is determined by

$$\xi(j\Delta\xi,\mathrm{IP})=x_{\mathrm{bin}}\cos\left(\gamma_{\mathrm{IP}}(j\Delta\xi)\right)+y_{\mathrm{bin}}\sin(\gamma_{\mathrm{IP}}(j\Delta\xi)),\tag{A.17}$$

where $(x_{\mathrm{bin}},y_{\mathrm{bin}})$ is the coordinate of the exit detector bin $j\Delta\xi$ on the rear tracker in the image space $(x,y)$. The determination of $F(j\Delta\xi,\mathrm{IP})$ is demonstrated in figure A4. This process is similar to transforming parallel beam projections to fan beam projections, where $(x_{\mathrm{bin}},y_{\mathrm{bin}})$ can be considered the source point. The set of angles is quite irregular though, depending on the object hull.

## ORCID iDs

Reinhard W Schulte https://orcid.org/0000-0002-7892-2756

## References


Agostinelli S *et al* 2003 Geant4—a simulation toolkit *Nucl. Instrum. Methods* A **506** 250–303
Bartolac S and Jaffray D 2013 Compensator models for fluence field modulated computed tomography *Med. Phys.* **40** 121909
Bartolac S, Graham S, Siewerdsen J and Jaffray D 2011 Fluence field optimization for noise and dose objectives in CT *Med. Phys.* **38** S2–S17
Bashkirov V, Schulte R W, Hurley R, Johnson R, Sadrozinski H W, Zatserklyaniy A, Plautz T and Giacometti V 2016 Novel scintillation detector design and performance for proton radiography and computed tomography *Med. Phys.* **43** 664–74
Bopp C 2014 The proton as a dosimetric and diagnostic probe *PhD Thesis* Université de Strasbourg
Buzug T M 2008a *Computed Tomography: from Photon Statistics to Modern Cone-Beam CT* (Berlin: Springer)
Buzug T M 2008b Two-dimensional fourier-based reconstruction methods *Computed Tomography: from Photon Statistics to Modern Cone-Beam CT* (Berlin: Springer) ch 5, pp 151–200
Cormack A M 1963 Representation of a function by its line integrals, with some radiological applications *J. Appl. Phys.* **34** 2722–7
Dedes G *et al* 2017 Application of fluence field modulation to proton computed tomography for proton therapy imaging *Phys. Med. Biol.* **62** 6026–43
Dedes G, Johnson R P, Pankuch M, Detrich N, Pols W M A, Rit S, Schulte R W, Parodi K and Landry G 2018 Experimental fluence-modulated proton computed tomography by pencil beam scanning *Med. Phys.* **45** 3287–96
Eyges L 1948 Multiple scattering with energy loss *Phys. Rev.* **74** 1534–5
Fekete C A C, Doolan P, Dias M F, Beaulieu L and Seco J 2015 Developing a phenomenological model of the proton trajectory within a heterogeneous medium required for proton imaging *Phys. Med. Biol.* **60** 5071
Fermi E 1940 The ionization loss of energy in gases and in condensed materials *Phys. Rev.* **57** 485–93
GEANT-Collaboration *et al* 2017 Physics reference manual Version: geant4 10.4 (http://geant4-userdoc.web.cern.ch/geant4-userdoc/UsersGuides/PhysicsReferenceManual/fo/PhysicsReferenceManual.pdf)
Giacometti V *et al* 2017 Software platform for simulation of a prototype proton CT scanner *Med. Phys.* **44** 1002–16
Gore J C and Tofts P S 1978 Statistical limitations in computed tomography *Phys. Med. Biol.* **23** 1176–82
Gottschalk B 2010 On the scattering power of radiotherapy protons *Med. Phys.* **37** 352–67
Gottschalk B 2012 Techniques of proton radiotherapy: transport theory (arXiv:1204.4470)
Graham S, Siewerdsen J and Jaffray D 2007 Intensity-modulated fluence patterns for task-specific imaging in cone-beam CT *Medical Imaging 2007: Physics of Medical Imaging* vol 6510 (International Society for Optics and Photonics) p 651003
Hansen D C, Sørensen T S and Rit S 2016 Fast reconstruction of low dose proton CT by sinogram interpolation *Phys. Med. Biol.* **61** 5868
Huesman R, Gullberg G, Greenberg W and Budinger T 1977 Users manual: donner algorithms for reconstruction tomography *Technical Report* PUB-214 1977 (Berkeley, CA: Lawrence Laboratory)
Huesman R H 1984 A new fast algorithm for the evaluation of regions of interest and statistical uncertainty in computed tomography *Phys. Med. Biol.* **29** 543
Ivanchenko V, Kadri O, Maire M and Urban L 2010 Geant4 models for simulation of multiple scattering *J. Phys.: Conf. Ser.* **219** 032045
Kak A and Slaney M 1988 *Principles of Computerized Tomographic Imaging* (Piscataway, NJ: IEEE)
Koivula L, Wee L and Korhonen J 2016 Feasibility of MRI-only treatment planning for proton therapy in brain and prostate cancers: dose calculation accuracy in substitute CT images *Med. Phys.* **43** 4634–42
Li T, Liang Z, Singanallur J V, Satogata T J, Williams D C and Schulte R W 2006 Reconstruction for proton computed tomography by tracing proton trajectories: a Monte Carlo study *Med. Phys.* **33** 699–706
Maspero M, Van den Berg C A, Landry G, Belka C, Parodi K, Seevinck P R, Raaymakers B W and Kurz C 2017 Feasibility of MR-only proton dose calculations for prostate cancer radiotherapy using a commercial pseudo-CT generation method *Phys. Med. Biol.* **62** 9159
Meyer S, Gianoli C, Magallanes L, Kopp B, Tessonnier T, Landry G, Dedes G, Voss B and Parodi K 2017 Comparative Monte Carlo study on the performance of integration- and list-mode detector configurations for carbon ion computed tomography *Phys. Med. Biol.* **62** 1096
Molière G 1947 Theorie der Streuung schneller geladener Teilchen I—Einzelstreuung am abgeschirmten Coulomb-Feld *Z. Nat.forsch.* A **2** 133–45
Molière G 1948 Theorie der Streuung schneller geladener Teilchen II—Mehrfach- und Vielfachstreuung *Z. Nat.forsch.* A **3** 78–97
Paganetti H 2012 Range uncertainties in proton therapy and the role of Monte Carlo simulations *Phys. Med. Biol.* **57** R99
Payne M G 1969 Energy straggling of heavy charged particles in thick absorbers *Phys. Rev.* **185** 611–23
Penfold S, Rosenfeld A B, Schulte R and Schubert K 2009 A more accurate reconstruction system matrix for quantitative proton computed tomography *Med. Phys.* **36** 4511–8
Penfold S, Schulte R W, Censor Y and Rosenfeld A B 2010 Total variation superiorization schemes in proton computed tomography image reconstruction *Med. Phys.* **37** 5887–95
Poludniowski G, Allinson N and Evans P 2014 Proton computed tomography reconstruction using a backprojection-then-filtering approach *Phys. Med. Biol.* **59** 7905
Quiñones C T 2016 Proton computed tomography *PhD Thesis* L'Institut National des Sciences Appliquées de Lyon
Ramachandran G N and Lakshminarayanan A V 1971 Three-dimensional reconstruction from radiographs and electron micrographs: application of convolutions instead of Fourier transforms *Proc. Natl Acad. Sci.* **68** 2236–40
Rank C M, Hünemohr N, Nagel A M, Röthke M C, Jäkel O and Greilich S 2013 MRI-based simulation of treatment plans for ion radiotherapy in the brain region *Radiother. Oncol.* **109** 414–8
Rinaldi I, Brons S, Gordon J, Panse R, Voss B, Jäkel O and Parodi K 2013 Experimental characterization of a prototype detector system for carbon ion radiography and tomography *Phys. Med. Biol.* **58** 413
Rit S, Dedes G, Freud N, Sarrut D and Létang J M 2013 Filtered backprojection proton CT reconstruction along most likely paths *Med. Phys.* **40** 031103
Sadrozinski H W *et al* 2016 Operation of the preclinical head scanner for proton CT *Nucl. Instrum. Methods Phys. Res.* A **831** 394–9
Schulte R, Penfold S, Tafas J and Schubert K 2008 A maximum likelihood proton path formalism for application in proton computed tomography *Med. Phys.* **35** 4849–56
Schulte R W *et al* 2005 Density resolution of proton computed tomography *Med. Phys.* **32** 1035–46

Schäfer D, van de Haar P and Grass M 2015 Fully 3d variance reconstruction for circular cone beam CT *The 13th Int. Meeting on Fully Three-Dimensional Image Reconstruction in Radiology and Nuclear Medicine* pp 174–7

Shunhavanich P, Bennett N R, Hsieh S S and Pelc N J 2018 Implementation of a piecewise-linear dynamic attenuator *Medical Imaging 2018: Physics of Medical Imaging* vol 10573 (International Society for Optics and Photonics) p 105730T

Stayman J W, Mathews A, Zbijewski W, Gang G, Siewerdsen J, Kawamoto S, Blevis I and Levinson R 2016 Fluence-field modulated x-ray CT using multiple aperture devices *Medical Imaging 2016: Physics of Medical Imaging* vol 9783 (International Society for Optics and Photonics) p 97830X

Szczykutowicz T and Mistretta C 2014 Experimental realization of fluence field modulated CT using digital beam attenuation *Phys. Med. Biol.* **59** 1305

Szczykutowicz T P and Mistretta C A 2013a Design of a digital beam attenuation system for computed tomography: part I. system design and simulation framework *Med. Phys.* **40** 021905

Szczykutowicz T P and Mistretta C A 2013b Design of a digital beam attenuation system for computed tomography. Part II. performance study and initial results *Med. Phys.* **40** 021906

Szczykutowicz T P, Hermus J, Geurts M and Smilowitz J 2015 Realization of fluence field modulated CT on a clinical tomotherapy megavoltage CT system *Phys. Med. Biol.* **60** 7245

Taasti V T *et al* 2018 Inter-centre variability of CT-based stopping-power prediction in particle therapy: survey-based evaluation *Phys. Imaging Radiat. Oncol.* **6** 25–30

Tanaka S, Nishio T, Tsuneda M, Matsushita K, Kabuki S and Uesaka M 2018 Improved proton CT imaging using a bismuth germanium oxide scintillator *Phys. Med. Biol.* **63** 035030

Taylor J *et al* 2016 An experimental demonstration of a new type of proton computed tomography using a novel silicon tracking detector *Med. Phys.* **43** 6129–36

Tschalär C 1968a Straggling distributions of extremely large energy losses *Nucl. Instrum. Methods* **64** 3

Tschalär C 1968b Straggling distributions of large energy losses *Nucl. Instrum. Methods* **61** 141–56

Wunderlich A and Noo F 2008 Image covariance and lesion detectability in direct fan-beam x-ray computed tomography *Phys. Med. Biol.* **53** 2471

Yang M, Zhu X R, Park P C, Titt U, Mohan R, Virshup G, Clayton J E and Dong L 2012 Comprehensive analysis of proton range uncertainties related to patient stopping-power-ratio estimation using the stoichiometric calibration *Phys. Med. Biol.* **57** 4095

Zhang Y and Ning R 2008 Investigation of image noise in cone-beam CT imaging due to photon counting statistics with the Feldkamp algorithm by computer simulations *J. X-Ray Sci. Technol.* **16** 143–58